EXPLORING LATE DEVONIAN MASS EXTINCTIONS AND OCEAN ANOXIA EVENTS IN
UNDERSTUDIED PALEOENVIRONMENTS OF ASIA

by

Olivia C. Paschall

Honors Thesis

Appalachian State University

Submitted to the Department of Geological and Environmental Sciences
and The Honors College
in partial fulfillment of the requirements for the degree of

Bachelor of Science

December, 2018

Approved by:

_____
Sarah K. Carmichael, Ph.D., Thesis Director

_____
Bob F. Swarthout, Ph.D., Second Reader

_____
Cole T. Edwards, Ph.D., Departmental Honors Director

_____
Jefford Vahlbusch, Ph.D., Dean, The Honors College

Contents

Acknowledgements

I would like to thank Dr. Sarah Carmichael and Dr. Johnny Waters for their continued support and encouragement on this project and throughout my undergraduate education in general. They have inspired me to become a better and more confident researcher, scientist, and explorer. My success would absolutely not be possible without their patience and guidance. I can only hope to become a research scientist and educator of their caliber. Thank you to Peter Königshof, for collecting the Cat Ba samples for geochemical analysis and continued support regarding conodont biostratigraphy. Thank you to our field team in Mongolia for a productive research expedition and wonderful experience with international collaborators: Dr. Sersmaa Gonchigdorj, Dr. Ariunchimeg Yarinpil, Otgonbaatar Dorjsuren, Tumurchudor Choimbol, Ganbayar Guunchinbat, Otgonbayar Nerkhjav, Will Waters, and everyone on the Mongolian field support team. Thank you to Dr. Bob Swarthout for being the second reader of my thesis and for providing insightful feedback. I would like to thank my research partner-in-crime Allison Dombrowski for encouragement and companionship in Mongolia as well as during late nights in Rankin. Thank you to my sources of funding, including Appalachian State University, Southeastern Section of the Geological Society of America, American Association of Petroleum Geologists, and the Explorers Club. Thank you to Anthony Love for patient guidance on preparing samples for SEM analysis. Thank you to my wonderful support system, including but not limited to: my parents, Devin Hoffman, Kevin Bynum, Delaney Ryan, and Victoria Haynes.

Abstract

The Devonian-Carboniferous (D-C) transition (359 Ma) was a period of rapid global faunal changes in conjunction with global cooling and widespread ocean anoxia. The end-Devonian mass extinction is one of the top 10 mass extinctions in Earth's history, and the associated anoxia and regression is referred to as the Hangenberg Crisis. In many locations, the Hangenberg Crisis is characterized in the rock record by sandstone and black shale deposits. Little is known about the Hangenberg Crisis in Southeast Asia, however. Here we show that the Hangenberg Crisis is recorded within the Pho Han Formation on Cat Ba Island in northeastern Vietnam, and at the Hoshoot Shiveetiin Gol locality in the Hovd Province of southwest Mongolia.

Preliminary work in July-August 2018 at the Hoshoot Shiveetiin Gol locality in Mongolia reveals that the Late Devonian shallow marine sequence is relatively continuous and encompasses the entire Late Devonian timescale, including both the Frasnian-Famennian and Devonian-Carboniferous transitions. Although no black shale is present at the locality due to the location's paleotopography, we interpret a pronounced arkosic sandstone layer to represent the Hangenberg regression event.

In contrast, the Cat Ba Island section in Vietnam represents a sediment-starved basinal facies on the South China carbonate platform, where long-term dysoxic/anoxic conditions (as determined by trace element proxies, increased total organic carbon, and framboidal pyrite distributions) persisted. More severe anoxia (approaching euxinia) exists within the Hangenberg Crisis stratigraphic interval. Mercury (Hg) chemostratigraphy reveals a significant enrichment that corresponds to the Hangenberg Crisis and the D-C transition. The Hg is most likely sourced from volcanic emissions, potentially linking the end-Devonian anoxia and mass extinction to large-scale volcanic activity. This is a new and valuable

development that is supported by very recent studies in Uzbekistan and Germany and must be investigated further. As both sites represent the two end members of understudied paleoenvironments (compared to sites in Europe and North America, where overlapping signals can be difficult to interpret), they are critical to understanding Late Devonian anoxia and extinction events.

Preface

       This thesis is a product of the research I have completed over the past three years with the DAGGER (Devonian Anoxia, Geochemistry, Geochronology, and Extinction Research) research group. We are an international and interdisciplinary research team affiliated with the UNESCO International Geoscience Programme's (IGCP) Projects 580, 596, and 652. Our team primarily studies two stages of Late Devonian ocean anoxia and mass extinction events: the Frasnian-Famennian extinction (372 Ma) which corresponds to the Kellwasser anoxia event, and the Devonian-Carboniferous extinction (359 Ma) which corresponds to the Hangenberg anoxia event/crisis. These extinction events are collectively called the Late Devonian mass extinction, which is one of the "big five" mass extinctions in Earth history (Raup and Sepkoski, 1982; McGhee, 2013), but it is arguably the least understood of them. Unlike the other massive extinction events, no single trigger is apparent, and our understanding of Late Devonian anoxia events is limited by concentrated study locations in North America and Europe (which were geographically adjacent during the Devonian as Pangaea was forming). The depositional histories at these sites that were situated on the Euramerican continent are complicated by the building and shedding of the Appalachian Mountains during the Variscan/Appalachian orogeny. For this reason, the DAGGER team studies unique and underrepresented paleogeographic locations that are independent of this orogenic event. My thesis incorporates research from two locations in Asia, where relatively little is known about the Late Devonian anoxia and extinction events (Fig. P-1). These two locations represent endmembers in terms of depositional settings: the first being an open ocean island arc complex, and the second representing a restricted basin *not* being affected by mountain building/shedding that often overprints true ocean anoxia signatures. The lithologies that define the Hangenberg Crisis in these locations are

very different when compared to the type section in Germany, which preserves a very specific and unusual paleoenvironment.

Part I of my thesis is based on 2018 fieldwork in the Khovd Province of Mongolia. Previous fieldwork in 2012 and 2014 was completed by DAGGER members. The field site of particular interest to this study is called Hoshoot Giveetiin Gol, which contains Late Devonian stratigraphy that records the events associated with both the Frasnian-Famennian and Devonian-Carboniferous boundaries. My job in the field was to make a geologic map of the site in order to assess the usefulness of radiometric dating of a basalt flow, as well as to determine if the section is stratigraphically continuous in the area of interest. This will serve as a jumping off point for studies by future DAGGER members, who will use multi-proxy geochemical and lithological analyses, similar to those used in Part II of this thesis.

Part II of this thesis focuses on a stratigraphic section at Cat Co Beach on Cat Ba Island in northeastern Vietnam. This section includes and expands upon my first-author manuscript that has been submitted to the journal *Global and Planetary Change*. The manuscript is entitled "The Devonian-Carboniferous boundary in Vietnam: sustained ocean anoxia with a volcanic trigger for the Hangenberg Crisis?" The purpose of this study was to investigate how the Hangenberg Crisis is recorded in a historically anoxic basin, both geochemically and lithologically. The lithologic section was described and analyzed for conodont biostratigraphy in Komatsu et al. (2014), and my study is a geochemical and mineralogical continuation of this work. I used geochemical, principle component, and framboidal pyrite analyses to locate and interpret the severity of the Hangenberg Crisis within the section. Investigating mercury chemostratigraphy allowed me to propose widespread volcanism as a potential trigger of the Hangenberg Crisis.

Preface Figure
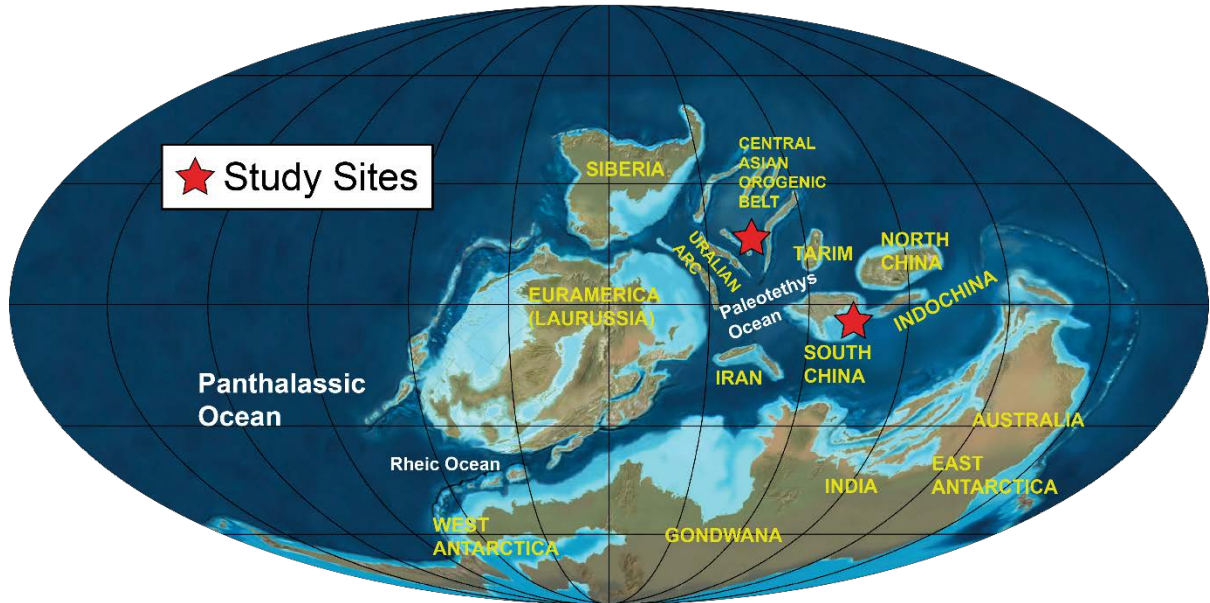
Figure P-1. Paleogeographic reconstruction of the continents during the Late Devonian with thesis study locations in red. Most Late Devonian study locations were within Euramerica during the Devonian. Figure modified from Blakey (2016), using updated paleogeographic data for Asia from Xiao et al. (2010) and Metcalfe (2009).

Part I

MAPPING LATE DEVONIAN MASS EXTINCTIONS AND ANOXIA EVENTS AT THE

HOSHOOT SHIVEETIIN GOL LOCALITY IN THE KHOVD PROVINCE OF MONGOLIA

1. Introduction

The discovery of anoxia indicators in the West Junggar island arc in northwest China (part of the Central Asian Orogenic Belt, or CAOB) was the first of its kind to demonstrate that late Devonian anoxia was global in scope and likely due to shallow water eutrophication (Carmichael et al., 2014, 2016). Carmichael et al. (2014, 2016) put forward a new mechanism for ocean anoxia that is climate-driven and can explain the global anoxia phenomena, contradicting the previous hypothesis of upwelling anoxic waters in shallow continental seas and shelf regions (Algeo et al., 2007; Caplan and Bustin, 1999; Caplan et al., 1996; Cramer et al., 2008; Formolo et al., 2014; Komatsu et al., 2014; Smith and Bustin, 1998). Previous study locations are primarily located in North America, Northern Africa, and Europe, which were paleogeographically adjacent during the Late Devonian. Interpretations of sediment deposition in these locations are moderated by concurrent Appalachian/Variscan mountain building and shedding (Averbuch et al., 2005; Carmichael et al., in review).

For example, the biostratigraphy defining the D-C boundary is based on the Global Stratotype Section and Point (GSSP) location La Serre Trench E'section at Montagne Noire, France, but there is debate whether these sediments are correlatable to other sections due to potential sediment reworking (Corradini et al., 2017; Spalletta et al., 2017). Conodont biostratigraphy is not the only issue when correlating D-C sediments to other paleogeographic locations; lithologies marking the Hangenberg Crisis are also widely varied.

Within epicontinental basins and continental margins, two lithologies record the event: (1) the Hangenberg black shale (HBS), and (2) the regressive Hangenberg sandstone (HSS) or unconformity, related to growth of continental ice sheets (Bábek et al., 2016; Cole et al., 2015; Becker et al., 2016; Kaiser et al., 2015). However, the same lithologic and taxonomic trends are difficult if not impossible to compare to independent paleoenvironmental settings, such as an open ocean island arc complex like the one presented here (Suttner et al., 2018 (accepted)) or in China (Carmichael et al, 2016). For this reason, new study sites entirely independent of previous study locations are necessary to test the hypothesis put forward in Carmichael et al. (2016).

A new location to test this hypothesis was found when an expedition to southwestern Mongolia in 2012 suffered an accident when one of the vans in the caravan flipped onto its side while backing down a road. Part of the crew explored the outcrops in the area while the van was righted and fixed; they discovered an excellently-preserved, relatively continuous Late Devonian shallow marine sequence in the meantime (Kido et al., 2013). This locale is called Hoshoot Shiveetiin Gol, which was deposited within the East Junggar arc in the CAOB. The group returned in 2014 for additional sampling for biostratigraphy and sampling for zircon geochronology (Thomas et al., 2017). Preliminary biostratigraphy shows the site to be Famennian in age (Suttner et al, in revision), but little else was known before our field expedition in summer 2018. Additional sampling and geologic mapping were necessary to find evidence of ocean anoxia events and constrain the stratigraphic location of the Frasnian-Famennian (F-F) transition and look for the Devonian-Carboniferous (D-C) boundary.

In 2014, the basaltic/andesitic lava flow that was discovered at the field site provided a potential zircon source for radiometric dating (Thomas et al., 2017). However, the relationship between the lava flow and the exposed Famennian shallow marine stratigraphic

sequence was unknown. The area is structurally complex, and any unmapped faults in the area could potentially eliminate the usefulness of a radiometric age from the lava flow. Alternatively, if the lava flow was structurally continuous with the beach sediments used for detailed conodont biostratigraphy, the radiometric age could be used in conjunction with biostratigraphy to obtain a more accurate depositional age. In addition, it would allow us to constrain the stratigraphic positions of the Kellwasser and Hangenberg Events. Another motivation for determining the structural relationship of rocks in the area was to ascertain the usefulness of Sr isotope values. They are important either for recording the signature of groundwater discharge from the terrestrial sediments into the surrounding fringe reefs, or for helping us understand the oceanic conditions during deposition (as described for the sediments on the West Junggar Arc by Carmichael et al., 2017).

We answered these questions in July-August 2018 as part of our expedition to the Hoshoot Shiveetiin Gol locality, when we mapped the study site and the surrounding area. Here we show that the lava flow is stratigraphically continuous with the shallow marine sequence, the Hangenberg regression event is recorded as an arkosic sandstone, and that multi-proxy geochemical and lithological analysis (similar to that in Part II of this thesis) will be critical to assess the severity of the marine anoxia events and mass extinctions preserved at Hoshoot Shiveetiin Gol.

2. Materials and Methods

Topographic maps (45.264°N - 45.274°N, 91.04°E - 91.06°E) of the field site were produced using Generic Mapping Tools (GMT) (Fig. I-1). Prior to creating these maps, the only existing topographic maps of our field site were 1:240,000 scale Russian maps, which are insufficient for m-scale geologic mapping. The digital elevation model (DEM) data were retrieved from the U.S. Geological Survey (USGS) Earth Explorer website. The 1 arc-second DEM data were collected by the NASA Shuttle Radar Topography Mission (SRTM), and the topographic maps produced with these data were used for geologic mapping in the field. The primary topography map used in the field is shown in Fig. I-1, with previously-collected samples (from 2014) shown in red triangles which were used for reference.

Our geologic field map of the Hoshoot Shiveetiin Gol field site was produced using standard geologic mapping techniques. We used rock hammers, Brunton compasses, and handheld GPS units with precision within ~3 m (Garmin GPSMAP 64). Strike and dip measurements and GPS coordinates were taken at each mapping site. We collected lithologic, bedding orientation, and additional observational data from over 80 stops (see Table I-2) in order to create a meter-scale geologic map of the field site.

Other team members at Hoshoot Shiveetiin Gol recorded detailed stratigraphy data and collected samples for conodont biostratigraphy and chemostratigraphy; collected fossil samples including rugose corals, echinoderms, and bivalves; and performed km-scale mapping of the region (including but not limited to Hoshoot Shiveetiin Gol).

3. Results

We defined eight geologic mapping units (described in Table I-1), and the field data collected at Hoshoot Shiveetiin Gol are recorded in Table I-2. Our preliminary interpretations are presented in the geologic field map in Fig. I-2. We inferred a fault via large-scale satellite images (provided by Mongolian colleagues), and our interpretations were digitized and further refined by overlaying field data with satellite images in Adobe Illustrator (Fig. I-3). A large antiform trending ENE is the dominant structural feature in the mapping area. Based on lithology and conodont biostratigraphy (personal communication, Peter Königshof), this feature is a plunging syncline. Our map (Fig. I-3) reveals that the sedimentary units are continuous except for the one fault which only offsets the units by ~50 m or less.

The base of unit ark1 is composed of coarse-grained arkosic sandstone with local conglomerate lenses and plant fossils (see Table I-1), which we interpret as the Hangenberg sandstone and regression event. This rock unit marks the base of the Carboniferous, an interpretation supported by the presence of plant fossils (that have not been taxonomically classified at this time). Therefore, the detailed sedimentary logs represented as lines "HS-1" to "HS-16f" and "HS-W" (standing for Hoshoot Shiveetiin 1-16f and Hoshoot Shiveetiin-west, respectively) can be correlated with one another to create a stratigraphic section crossing not only the F-F boundary, but also the D-C boundary. This stratigraphic correlation and detailed lithologic logs were completed by colleagues Allison Dombrowski, Peter Königshof, and Sersmaa Gonchigdorj. Our m-scale map is also consistent with the km-scale mapping by team members Ariunchimeg Yarinpil, Otgonbaatar Dorjsuren, Tumurchudor Choimbol, Ganbayar Guunchinbat, and Otgonbayar Nerkhjav, shown in Figure I-5. The lava flow is located stratigraphically higher than the D-C boundary, making it Early Carboniferous in age, and therefore not an essential source of zircons for age dating.

13

4. Discussion

The Hoshoot Shiveetiin Gol site in the Devonian East Junggar Arc (within the CAOB) represents a unique paleogeographic location compared to other study locations within the epicontinental seaways and basins of Euramerica and northern Gondwana (Fig. P-1), meaning that there are few studies to use as direct comparison.

A few studies of Late Devonian island arc settings analogous to this study do exist, particularly in the Devonian West Junggar island arc (Carmichael et al., 2014; Carmichael et al., 2016; Kido et al., 2013; Suttner et al., 2014; Wang et al, 2016). The F-F Zhulumute and Hongguleleng Formations in Xinjiang, China are discussed in Suttner et al. (2014), Carmichael et al. (2014), and Wang et al (2016). These studies show that the typical black shale (seen in other paleogeographic locations, particularly Euramerica) is missing in island arc settings, and that there is no change in mineralogy across the F-F boundary (Carmichael et al., 2014; Suttner et al., 2014). Analysis of the D-C Heishantou Formation (also in in Xinjiang, China) shows that the Hangenberg Event is recorded on a steep slope, accreting island arc complex, even though no black shale (HBS) is present (Carmichael et al., 2016). An albite-rich siltstone/sandstone is present just above the interpreted D-C boundary (representing a marine regression) (Carmichael et al., 2016), which is analogous to the arkosic sandstone (the base of unit ark1) found at Hoshoot Shiveetiin Gol. We interpret this arkosic sandstone to be the HSS found in other paleogeographic locations. Our findings (in conjunction with work in Xinjiang, China) suggest that correlating sediments between island arc and epicontinental basin depositional settings, at least lithologically, is minimally useful.

Geochemical comparisons are more useful than lithologic comparisons for determining the presence of anoxia events (see Carmichael et al., 2014; Carmichael et al., 2016), but geochemical analyses have not yet been completed for Hoshoot Shiveetiin Gol sediments. This will be the next step of this research project that will be continued by other

members of the DAGGER research team, including Allison Dombrowski. Thorough analysis

of geochemical proxies (including PCA analysis) and presence/size distributions of pyrite

framboids (see Part II of this thesis for methodology) will be necessary to correlate this

section with other Late Devonian sections and to make more substantiated comparisons to

other studies.

5. Conclusions

Although our team expected to locate *only* the stratigraphic position of the F-F boundary via conodont biostratigraphy, we were in fact able to identify the HSS event in the field as the lithologies recorded a large-scale regression event and a marine to terrestrial transition. Based on our field mapping, the section is continuous, making the site a useful and potentially critical study location to show how the Kellwasser and Hangenberg Events are preserved in this paleogeographic setting and depositional environment. Radiometric dating of the basalt flow (unit lf in Table I-1 and Fig. I-3) may be unnecessary depending on the results of conodont biostratigraphy, allowing our study to move forward and focus on detailed geochemistry, cyclostratigraphy, and facies analysis, for example. The work outlined in Part I of this thesis comprises the preliminary work required for the multiproxy approach that is outlined for a different paleogeographic location in Part II.

Tables

Table I-1: Detailed rock descriptions of the units mapped at m-scale.

Unit Abbreviation	Unit Description
al	Alluvium and landslide deposits that include float consisting of basalt, breccia, conglomerate, greenstone, and microbialites.
slt3	Interbedded yellow-brown-green shale and black (weathered), gray-green (fresh) siltstone (beds ~20 cm thick) with some coarse sandstone to conglomerate (grains up to 3 mm diameter) layers, localized lava flows, and rare plant fossils
lf	Dark brown-black calc-alkalic vesicular basalt lava flow
cong1	Gray-brown (weathered), light gray-brown/tan (fresh) polymictic conglomerate (0.5-1 cm diameter clasts) with layers of dark brown-black and gray-green coarse sandstone and siltstone
ark1	Brown-gray with white speckles (weathered), whitish-gray (fresh) coarse-grained subangular to subrounded arkosic sandstone (~1 mm diameter grains) with local conglomerate lenses, contains plant fossils (lowermost Carboniferous)
cono	Green, yellow, and brown shale with fossiliferous limestone layers, many layers of volcanic ash (Frasnian and Famennian)
slt2	Light green-brown (weathered), light gray-green (fresh) siltstone with rare fossils, contains some mm-scale limestone beds and local limestone nodules
slt1	Brownish-gray-green with orange staining (weathered), dark gray-green (fresh) siltstone with varying bed thickness at cm scale

Table I-2: Data recorded in the field for m-scale mapping, including GPS coordinates, orientation of bedding, and unit or unit contact. Within the dip column, v = vertical and o = overturned.

Stop #	Latitude	Longitude	Strike	Dip	Unit or Contact
1	N 45.27287	E 91.05529	121	30	slt1
2	N 45.27271	E 91.05506	100	44	slt1-slt2 contact
3	N 45.27226	E 91.05465	111	45	slt2
4	N 45.27211	E 91.05441	095	47	slt2
5	N 45.27195	E 91.05438	082	50	slt2-cono contact
6	N 45.27179	E 91.05447	~090	-	ash layer in cono
7	N 45.27152	E 91.05420	101	54	cono
8	N 45.27148	E 91.05374	083	63	cono
9	N 45.27087	E 91.05316	065	63	cono-ark1 contact
10a	N 45.27083	E 91.05304	081	80	ark1
10b	N 45.27085	E 91.05299	084	60	ark1
10c	N 45.27079	E 91.05294	068	42	ark1
10d	N 45.27078	E 91.05305	095	79	ark1
10e	N 45.27076	E 91.05314	121	74	ark1(w/ plant fossils)
10f	N 45.27083	E 91.05325	155	58	ark1
11	N 45.27065	E 91.05321	-	-	ark1
12	N 45.27082	E 91.05289	050	50	ark1 (base)
13	N 45.27076	E 91.05244	055	30	ark1
14	N 45.27071	E 91.05188	084	46	ark1
15	N 45.27067	E 91.05162	063	61	ark1(w/ nodules)
16	N 45.27020	E 91.05071	-	-	slt3 conglomerate lens
17	N 45.27108	E 91.05004	110	55	ark1
18	N 45.27260	E 91.04904	107	49	cono (w/ crinoids)
19	N 45.27236	E 91.04889	123	46	cono (bryozoan bed)
20	N 45.27261	E 91.04926	118	62	cono
21	N 45.27266	E 91.04924	117	62	cono
22	N 45.27283	E 91.04954	119	66	cono
23	N 45.27294	E 91.04972	-	-	cono (crinoid layer)
24	N 45.27297	E 91.04992	114	53	cono-slt2 contact
25	N 45.27382	E 91.05052	-	-	basalt float, al
26	N 45.27404	E 91.05076	106	44	slt1-slt2 contact
27	N 45.27354	E 91.05098	080	64	slt2 (w/ nodules)
28	N 45.27162	E 91.04832	125	56	cong1-ark1 contact
29	N 45.27138	E 91.04832	-	-	cong1-slt3 contact
30	N 45.27107	E 91.04682	080	68	slt3
31	N 45.27435	E 91.04876	116	50	slt1
32	N 45.27405	E 91.04832	111	45	slt1-slt2 contact
33	N 45.27433	E 91.04872	120	54	slt2
34	N 45.27329	E 91.04768	-	-	cono
35	N 45.27293	E 91.04714	-	-	cono
36	N 45.27293	E 91.04714	-	-	ash layer in cono
37	N 45.27224	E 91.04663	090	55	ark1-cono contact

Stop #	Latitude	Longitude	Strike	Dip	Unit or Contact
38	N 45.27217	E 91.04646	085	46	ark1-cono contact
39	N 45.27202	E 91.04674	088	44	cong1-slt3 contact
40	N 45.27193	E 91.04633	-	-	basalt (float?)
41	N 45.27172	E 91.04629	-	-	basalt (float?)
42	N 45.27157	E 91.04622	080	32	basalt (float?)
43	N 45.27121	E 91.04991	124	60	cono-ark1 contact
44	N 45.27101	E 91.05006	108	45	ark1-cong1 contact
45	N 45.27049	E 91.05020	076	73	cong1-slt3 contact
46	N 45.26988	E 91.05050	-	-	basalt in slt3
47	N 45.27057	E 91.05190	-	-	ark1-cong1 contact
48	N 45.26867	E 91.05306	219	65	ark1
49	N 45.26888	E 91.05280	205	~v	ark1-cong1 contact
50	N 45.26897	E 91.05249	202	~v	ark1-cong1 contact
51	N 45.26940	E 91.05257	165	v	cong1
52	N 45.26959	E 91.05313	010	65	ark1-cono contact
53	N 45.27020	E 91.05330	185	56	ark1-cono contact
54	N 45.27041	E 91.05348	138	69	ark1-cono contact
55	N 45.27044	E 91.05251	010	62	ark1-cong1 contact
56	N 45.27012	E 91.05229	038	v	ark1
57	N 45.27004	E 91.05225	171	70	ark1-cong1 contact
58a	N 45.26979	E 91.05179	166	80	cong1
58b	N 45.26969	E 91.05184	155	80	cong1
58c	N 45.27002	E 91.05173	180	v	cong1
59	N 45.27010	E 91.05170	050	~v	cong1
60	N 45.26884	E 91.05161	-	-	vesicular basalt in cong1
61	N 45.26861	E 91.05198	~019	-	gabbro in cong1
62	N 45.26833	E 91.05145	009	85	cong1-slt3 contact
63	N 45.26777	E 91.05144	344	85o	cong1-slt3 contact
64	N 45.26664	E 91.05118	170	65	cong1-slt3 contact
65	N 45.26691	E 91.05219	195	45	cong1
66	N 45.26670	E 91.05247	196	65	cong1-ark1 contact
67	N 45.26633	E 91.05276	210	50	ark1-cono contact
68	N 45.26616	E 91.05267	207	65	cono
69	N 45.26616	E 91.05335	-	-	ash layer in cono
70	N 45.26617	E 91.05323	207	79	cono (w/ brachiopods)
71	N 45.26644	E 91.05397	213	75	cono
72	N 45.27175	E 91.05136	160	66	cono (w/ pyroclastic flow)
73a	N 45.27149	E 91.05145	141	60	cono
73b	N 45.27141	E 91.05153	104	52	cono
74	N 45.27154	E 91.05220	103	49	cono
75	N 45.27115	E 91.05406	070	56	ark1-cono contact
76a	N 45.27098	E 91.05406	200	~v	cono
76b	N 45.27090	E 91.05412	120	57	cono
76c	N 45.27092	E 91.05432	115	67	cono
76d	N 45.27065	E 91.05509	165	66	cono
76e	N 45.27050	E 91.05512	197	72	cono

Stop #	Latitude	Longitude	Strike	Dip	Unit or Contact
76f	N 45.27026	E 91.05486	040	75	cono
77	N 45.27063	E 91.05421	107	55	cono
78	N 45.27074	E 91.05403	127	56	cono
79	N 45.27044	E 91.05575	205	80	slt2 (w/ nodules)
80	N 45.27021	E 91.05601	032	v	slt2
81	N 45.27033	E 91.05621	215	75	slt2 (w/ fossiliferous bed)
82	N 45.27062	E 91.05634	167	72	slt2
83	N 45.27074	E 91.05638	165	59	slt2
84	N 45.27008	E 91.05674	214	74	slt1
W-1	N 45.27216	E 91.04814	105	44	ark1-cono contact
W-2	N 45.27283	E 91.04893	112	72	cono

Part I Figures
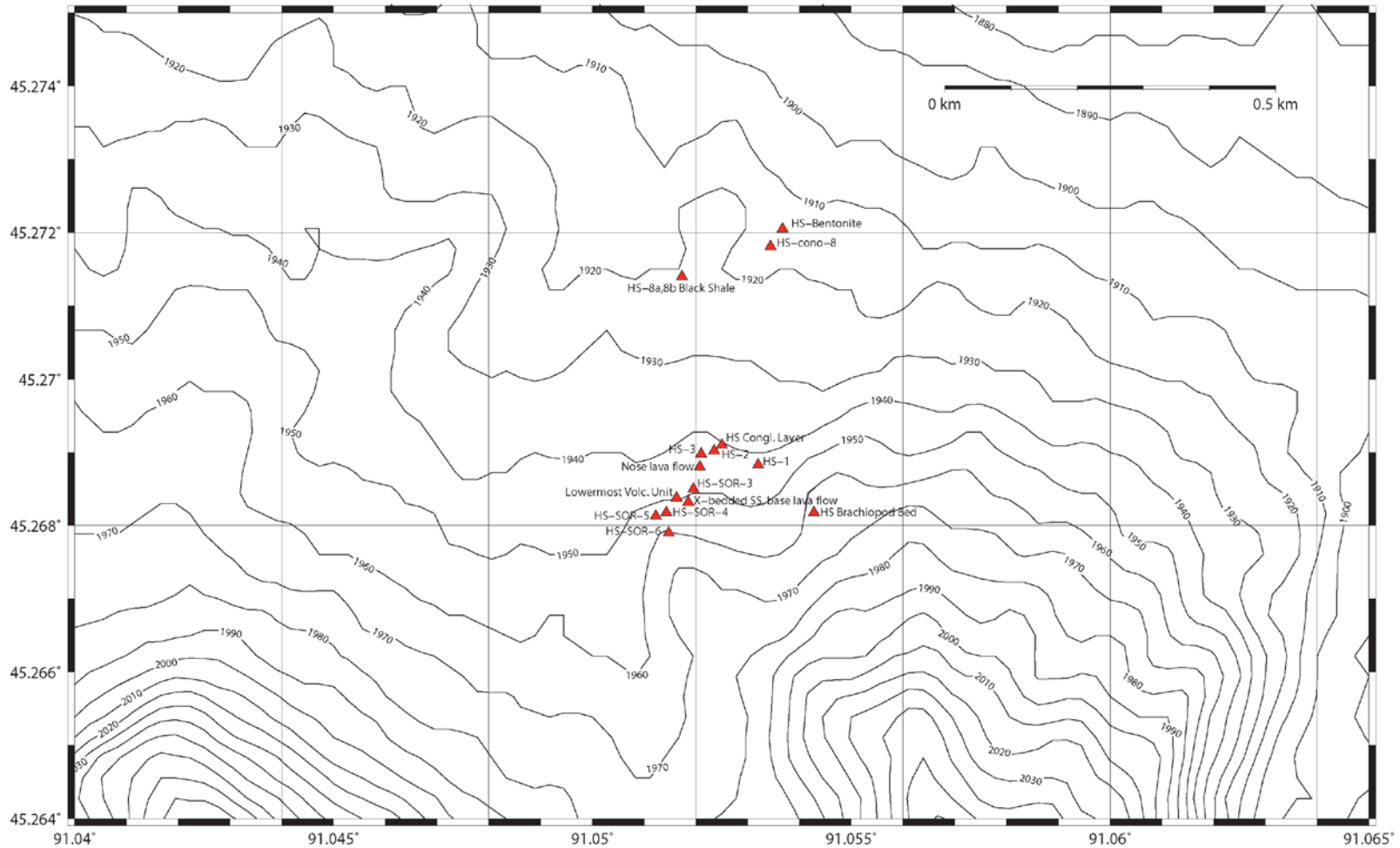
Figure I-1. Raw topography map of Hoshoot Shiveetiin Gol made in GMT prior to fieldwork. It includes sample names and locations from preliminary work completed in 2014. Contour intervals are 10 m. This map was used in the field as a basemap for manually recording bedding orientation and unit contact information.
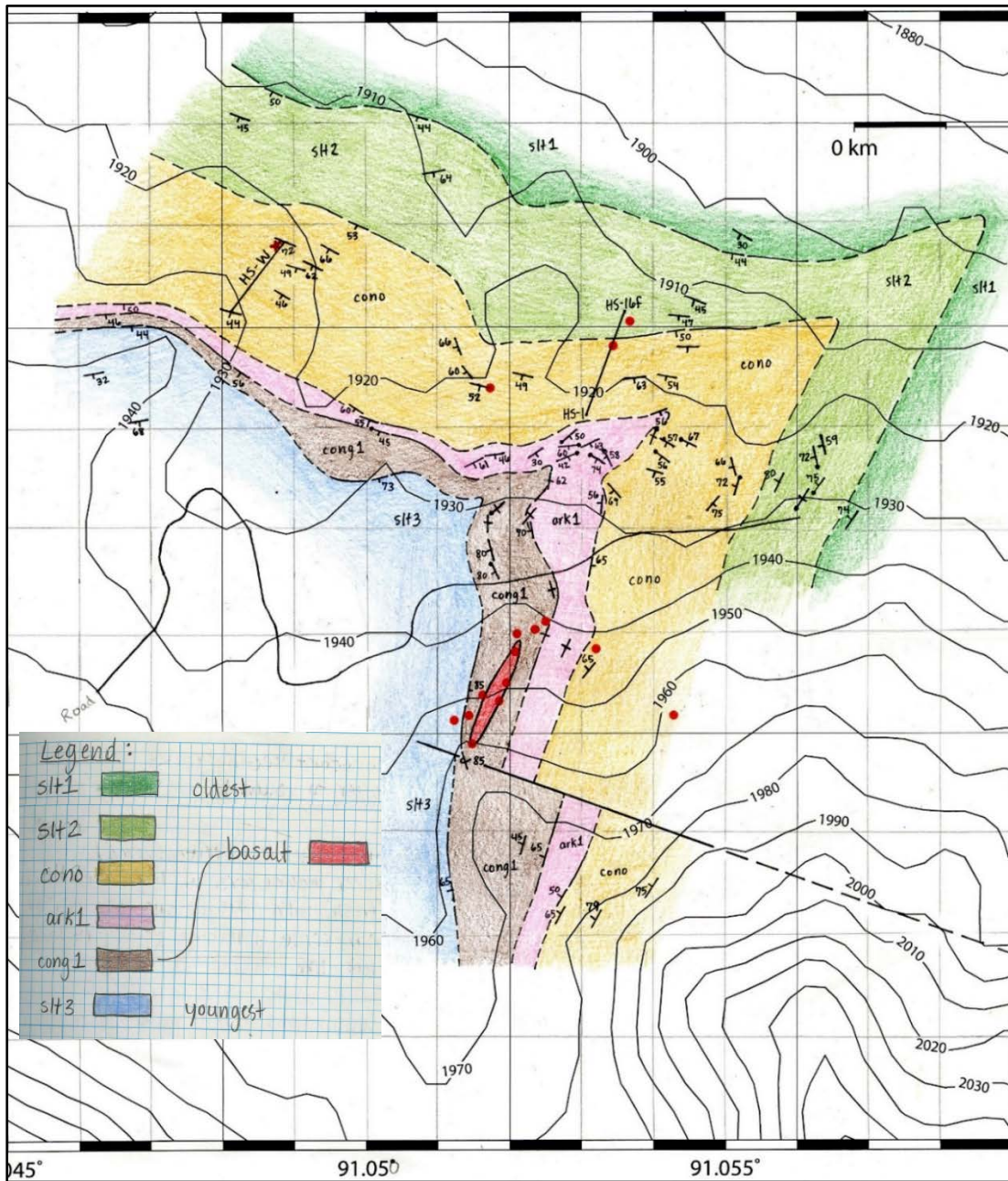
Figure I-2. Field map of Hoshoot Shiveetiin Gol field site using recorded data (found in Table 2) and large-scale satellite image (Fig. I-3). The legend was taken from my field notes, with the basalt being situated within unit cong1, indicated by the line connecting "basalt" to the cong1 unit. Red dots represent previous sample locations. See Fig. I-4 for finalized map. A fault is inferred from a satellite image we had in the field in the southern part of the mapped area, and detailed stratigraphic section locations are marked with black lines (labelled HS-1 to HS-16f and HS-W) (detailed stratigraphic logs produced by team members). Unit contacts and the fault are more clearly labelled in Fig. I-4.

Figure I-3. Satellite image of the locality, with the same dimensions as the topography map in Fig. 1. This was used in addition to field data (see Table I-2) to develop the final digitized map presented in Fig. I-4.
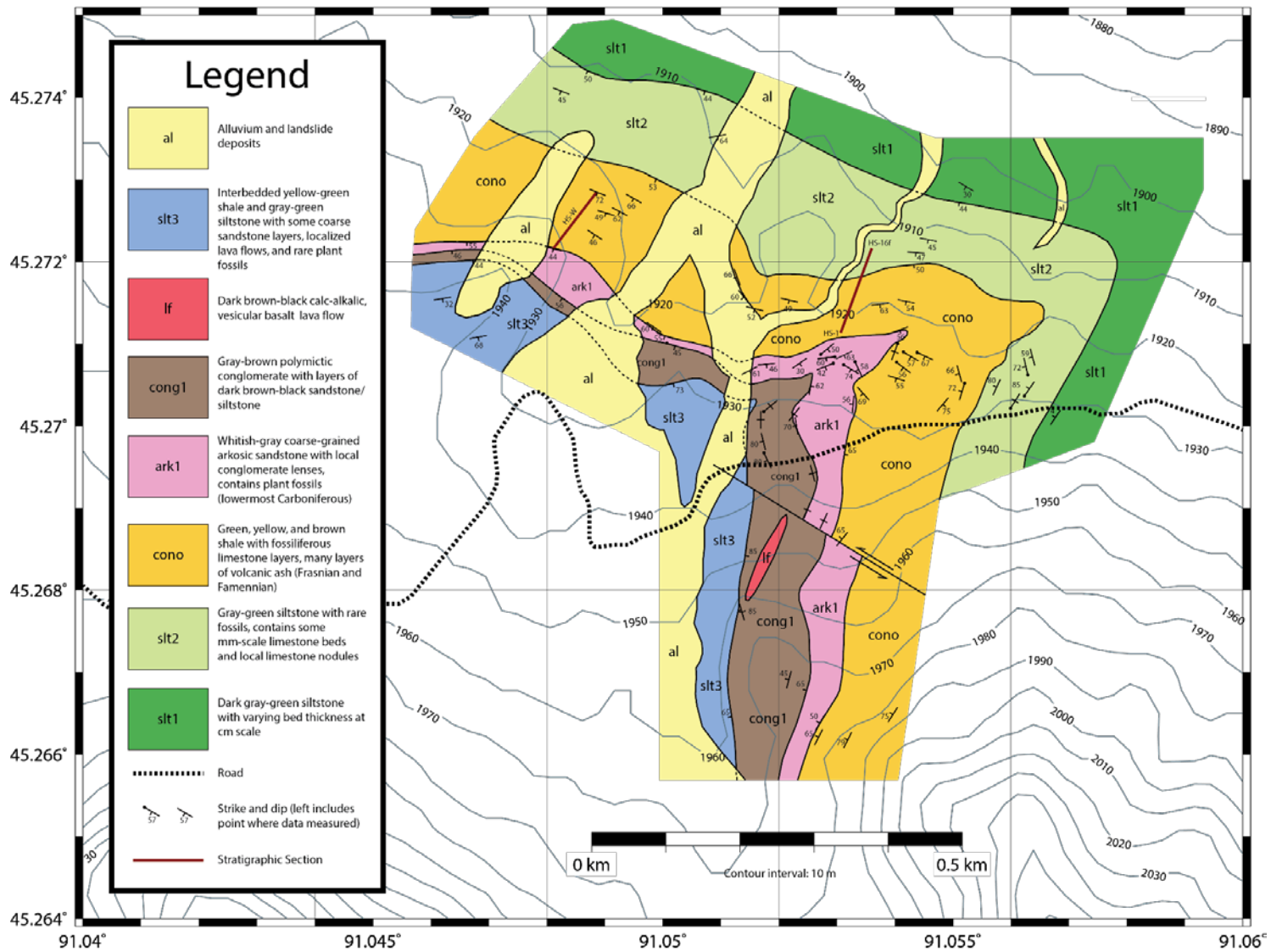
Figure I-4. Digitized and refined geologic map of Hoshoot Shiveetiin Gol.

24

GEOLOCAL MAP OF KHUSHUUT-SHIVEET AREA

Scale 1:25 000
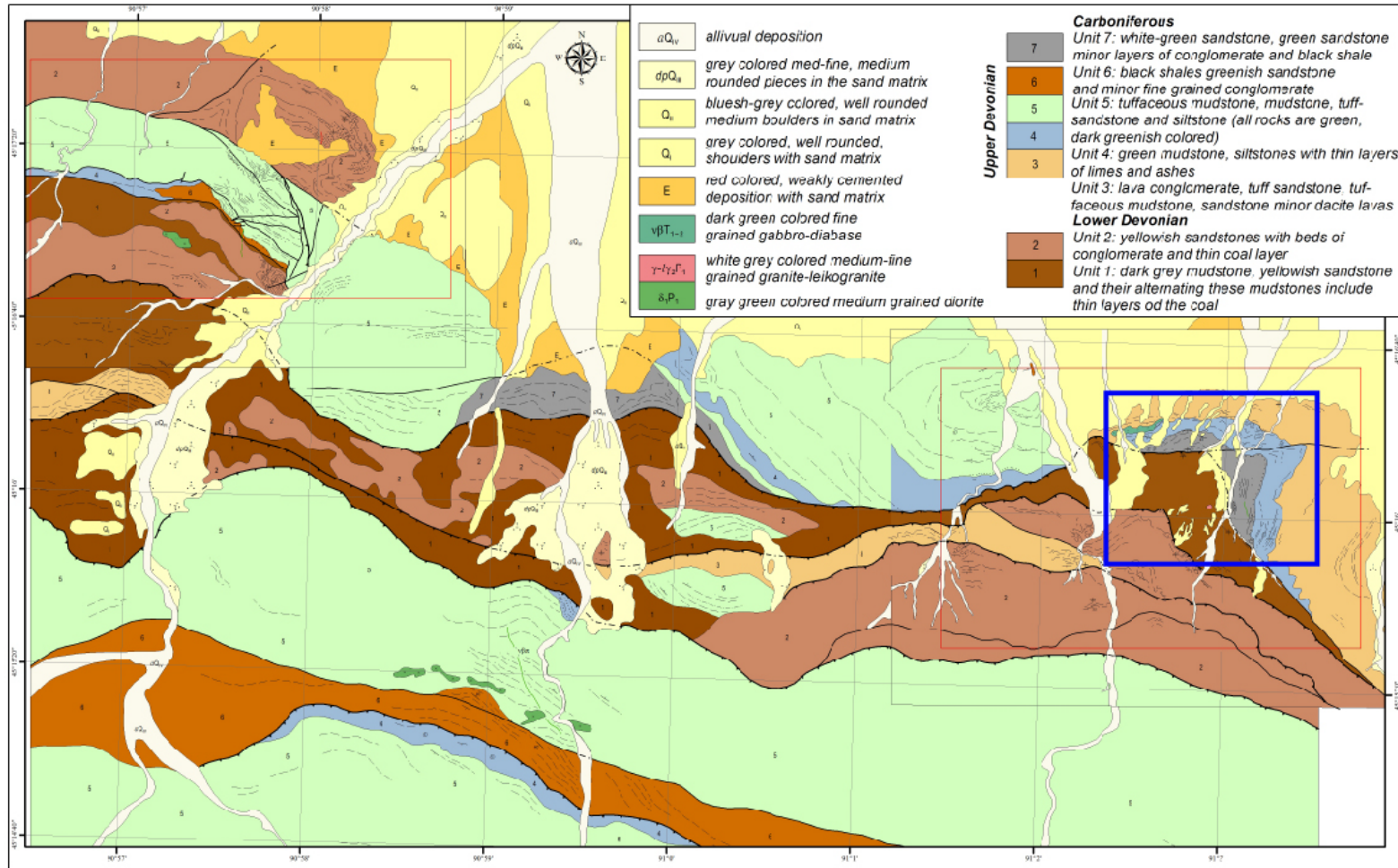
Figure I-5. km-scale geologic map made by team members Yarinpil, Dorjsuren, Choimbol, Guunchinbat, and Nerkhjav. Our focus area (Hoshoot Shiveetiin Gol) is outlined in blue.

Part II

THE DEVONIAN-CARBONIFEROUS BOUNDARY IN VIETNAM: SUSTAINED OCEAN

ANOXIA AND A POTENTIAL VOLCANIC TRIGGER FOR THE HANGENBERG CRISIS?

1. Introduction

The Devonian-Carboniferous (D-C) transition and mass extinction is characterized as a period of severe ecological crisis, with major biotic and palaeoenvironmental changes in both terrestrial and marine ecosystems. The extinction eliminated about 20% of marine invertebrate genera, such as trilobites, ammonoids, conodonts, and corals (Sandberg et al., 2002; Sepkoski, 1996; Walliser, 1996). The event primarily decimated pelagic organisms such as fish and cephalopods, reducing long-term biodiversity of all vertebrates by 50% (see reviews by Becker et al., 2016; Kaiser et al., 2015). The ecological severity index by McGhee et al. (2013) characterizes the end Devonian extinction as the fourth most severe mass extinction event in Earth's history.

Historically, the D-C boundary has been defined via conodont biostratigraphy from the Global Stratotype Section and Point (GSSP) location La Serre Trench E' section, Montagne Noire, France, with the first appearance of the basal Carboniferous conodont *Siphonodella sulcata* (Flajs and Feist, 1988; Paproth et al., 1991). However, these early siphonodellids are difficult to identify due to taxonomic uncertainties (Corradini et al., 2011), and the D-C boundary therefore needs to be reevaluated, either via new biostratigraphic indicators (Aretz, 2013; Corradini et al., 2017) or via a combined biostratigraphic and sedimentological set of criteria (Becker et al., 2016; Walliser, 1984).

The D-C transition is associated with not only a mass extinction, but also the Hangenberg ocean anoxia and regression event. The event is named for the Hangenberg Black Shale beds in the Rhenish Massif, Germany and has been recognized on

epicontinental basins or continental margins in Europe, North America, South China, and Morocco (Kaiser et al., 2015 and references therein) as well as in the Central Asian Orogenic Belt (Carmichael et al., 2016). The sedimentation of these locations can be complicated by tectonic overprinting associated with the Appalachian/Variscan orogenies or other local volcanism, and nearly all places where the Hangenberg Event has been studied to date are associated with sediments derived from cratons (see reviews by Becker et al., 2016; Kaiser et al., 2015).

The Hangenberg Crisis can be subdivided into the Hangenberg Black Shale Event (HBSE), and the regressive Drever Sandstone Event (at times only visible as an unconformity) (summarized in Kaiser et al., 2015). The HBSE is correlated with widespread deposition of black shale and is frequently (but not always) characterized by carbon isotope anomalies (Kaiser et al., 2015). The global regression associated with the Hangenberg Crisis appears to be related to continental icesheet growth as recorded by glacial sediments and palynomorph analyses in South America (Caputo et al., 2008; Isaacson et al., 1999; Streel et al., 2000), North Africa (summarized in Isaacson et al., 2008) and mountain glaciers in the Appalachians of North America (Brezinski et al., 2010; Brezinski et al., 2009). Aside from a general agreement regarding a glacially-influenced regression, the anoxia mechanisms that form the HBSE are still debated.

In fact, the processes and mechanisms of all of the Devonian ocean anoxia events (such as the Dasberg, Kellwasser, and Eifelian Events, as well as the HBSE) still remain contentious, as they likely represent a combination of long-term and short-term factors (see reviews by Carmichael and Waters, 2015; Kaiser et al., 2015; McGhee, 2001; McGhee, 2005; Racki, 2005). Long-term components of Late Devonian climate instability and changes in sediment/nutrient supply to the oceans include a dramatic decrease in atmospheric CO_2 via the evolution of complex land plant ecosystems, which increased the

amount of nutrients supplied to the oceans (Algeo et al., 1995; Algeo and Scheckler, 1998), along with active tectonic processes in the tropics that changed climate and wind/ocean currents, and provided nutrients (both siliciclastic and soils) to the oceans (Averbuch et al., 2005; Copper, 1986). Trigger mechanisms for these shorter pulses of Devonian anoxia may include orbital forcing (De Vleeschouwer et al., 2014; De Vleeschouwer et al., 2017; De Vleeschouwer et al., 2018; De Vleeschouwer et al., 2013), the presence of large igneous provinces (LIPs) (Bond and Wignall, 2014), or prolonged volcanic activity from a variety of sources (Racki et al., 2018). The Frasnian-Famennian extinction has now been correlated to a series of volcanic events through mercury chemostratigraphy (Racki et al., 2018).

It is important to recognize that most of the information about the Hangenberg Event is compiled from sites along tropical continental margins or within epicontinental basins, many of which were receiving increased sediment supply due to active tectonism during the late Famennian (Averbuch et al., 2005). This tectonic activity (Variscan/Appalachian orogeny) supplied increased amounts of sediments and nutrients to the oceans, potentially overprinting truly global signatures of anoxia with more localized signatures of eutrophication. The massive uplift also changed wind and ocean circulation patterns, changing local climates. For example, the German Standard D-C boundary at the Drewer Quarry is a famous example of the lithological preservation of the Hangenberg Crisis, but the deposition of these sediments was affected by active tectonism and only represents one specific paleoenvironmental setting.

As a step towards addressing this problem of sample bias, here we discuss the Hangenberg Event in a new location in Vietnam, in a sediment-starved carbonate basin that is associated with the South China continental block and was far from any tectonically or volcanically-derived source material, and we provide possible trigger mechanisms for the anoxia and extinction at the D-C boundary.

28

2. Regional Geology and Biostratigraphy

The Devonian to Carboniferous Pho Han Formation is exposed at the Cat Co 3 beach on Cat Ba Island, Hai Phong Province, northeastern Vietnam (Fig. II-1). The geologic setting and a detailed sedimentological description of the unit are described in detail in Komatsu et al. (2014). The Cat Co 3 section is unique because it is one of the few sections on the eastern South China continental block of the Paleotethys Sea (Fig. II-2) that preserves continuous deposition across the D-C boundary (Komatsu et al., 2014). At the Cat Co 3 beach section Cat Ba Island, the Pho Han Formation is approximately 500 m thick and consists of ramp platform carbonates and slope deposits (Doan and Tong-Dzuy, 2006; Komatsu et al., 2014; Komatsu et al., 2012; Ta Hoa and Doan, 2005; Ta Hoa and Doan, 2007). The depositional environment of these carbonates is interpreted as deep ramp to marginal basin plain, and primarily consists of alternating whitish gray to gray limestones, micritic limestones, and marls, with interbedded thin dark gray limestones and organic-carbon-rich black shales (Fig. II-3) (Komatsu et al., 2014). The alternations of thin dark gray limestone and black shale show no evidence of bioturbation, whereas the limestones are occasionally bioturbated (Komatsu et al., 2014). The fossil content of the carbonates is mainly composed of brachiopods, crinoid stems, conodont elements, and foraminifera (Komatsu et al., 2014).

The Cat Co 3 beach section spans the *Palmatolepis expansa* conodont zone to the *Siphonodella duplicata* conodont zone (Komatsu et al., 2014; Ta Hoa and Doan, 2005; Ta Hoa and Doan, 2007) (Fig. II-3). The prior standard Devonian-Carboniferous boundary definition is based on the first appearance of the conodont *Siphonodella sulcata* following the *Siphonodella praesulcata* subzone (Paproth et al., 1991; Sandberg et al., 1978; Ziegler and Sandberg, 1990). Bed 115c can be correlated with the Upper *Siphonodella praesulcata* subzone and *Siphonodella sulcata* appears for the first time in bed 119. Unfortunately,

29

conodonts are rare in beds 116-118 due to lithology. More recent work by Corradini et al.

(2017) instead suggests that the D-C boundary is placed between *Bispathodus ultimus* and

Protognathodus kockeli, with the base of the Carboniferous defined at the first appearance

of either *Protognathodus kockeli* or *Siphonodella bransoni*. In the Cat Co 3 beach section,

unfortunately, these conodonts were not found. Thus we place the D-C boundary

somewhere within beds 116-118.

 Beds 115b-120 (the alternating dark gray limestone and organic carbon-rich black

shales) were tentatively identified by Komatsu et al. (2014) as potential Hangenberg Crisis

markers as they have well-developed parallel laminations and no bioturbation. This study

therefore focuses on beds 104-125 of the original Komatsu et al. (2014) study, which

bracket the biostratigraphically constrained D-C transition and the expected location of the

Hangenberg Crisis.

3. Materials and Methods

Whole rock geochemical analyses (major, trace, and rare earth element (REE) geochemistry) were performed by Activation Laboratories in Ancaster, Ontario, Canada, using the Total IDENT 4E-Research package, with Code 1G-Hg CV Hg-Cold Vapour FIMS for Hg analyses. Total organic carbon (TOC) data was taken from Komatsu et al. (2014).

Carbon isotope analyses for both calcite and organic carbon ($\delta^{13}C_{carb}$ and $\delta^{13}C_{org}$) were performed in the GeoZentrum Nordbayern at the Friedrich-Alexander Universität Erlangen-Nürnberg, Erlangen, Germany. Calcite samples were powdered and mixed with 100% phosphoric acid at 70°C, and analyzed via a Gasbench II system with a ThermoFinnigan Delta Five Plus mass spectrometer. Carbon isotope analysis of organic carbon was performed using a Carlo-Erba1110 elemental analyzer coupled with to a ThermoFinnigan Delta Plus mass spectrometer. All values are reported in ‰VPDB.

Principal component analysis (PCA) was performed using program PAST 3.2 (Hammer et al., 2001) after geochemical data were converted to elemental weight percent and adjusted using the arcsine transform in Microsoft Excel. PCA was performed on whole-rock geochemical data, and repeated using trace elements only.

Samples were analyzed for mineralogy and framboidal pyrite distributions using a JEOL JSM-IT300LV scanning electron microscope (SEM) with an Oxford AZtecEnergy integrated silicon drift energy dispersive X-ray spectroscopy (EDS) system at the Dewel Microscopy Facility at Appalachian State University in Boone, NC. Automated feature detection, measurement, and analysis was done with the Oxford Aztec software to scan, count, and measure the diameters of pyrite framboids.

Two test samples (bed 110 and 121) were analyzed in order to determine an accurate yet efficient way to assess the size and distribution of pyrite framboids. Using the Features function in the Oxford Aztec EDS software, a 1 cm^2 area of the sample was

scanned with 0% frame spacing at 500X magnification (2028 photos), and framboids were

detected using a grayscale analysis of all features >2 μm in diameter. Samples were

analyzed again using a 100% frame spacing (520 photos, representing 0.26 cm^2 spread

evenly over 1 cm^2), under the same magnification and framboid detection conditions. The

resulting data were exported into Microsoft Excel for data analysis. For both samples, the

number of framboids counted using 0% spacing (all photos adjacent) vs. 100% spacing

(photos staggered by every other photo) are within 10% of each other, when the 100%

spacing framboid count was multiplied 4 to extrapolate the number of framboids per unit

area (1 cm^2). This process indicates that using 100% spacing when analyzing samples for

framboids is still within 10% of the actual value. As long as the number of framboids

exceeded 100 (for histogram analysis), we used 100% spacing during automation for time

purposes (2 hour analysis time vs. 8 hours for each sample). The distribution of framboid

sizes (length and equivalent circle diameter, or ECD) for 0 and 100% spacing were also

analyzed to ensure that the distribution was not affected by the reduction in frames. None of

the analyzed samples contained <100 framboids, so 100% spacing was used for all nine

representative samples.

Overall, statistical analysis of 0% grid spacing (100 mm^2 total analyzed area, using

2028 images) vs. 100% grid spacing (26.21 mm^2 total analyzed area, using 520 images)

shows that 100% spacing produces a framboid count and size distribution that is consistent

with 0% spacing. Therefore, 100% spacing was used for all nine representative Pho Han

samples, scanning an area of 26.21 mm^2 within 520 frames evenly spaced over a 1 cm^2

grid.

4. Results and Discussion

4.1. Geochemical Analyses

There is a major change in total organic carbon (TOC) and trace element geochemistry between beds 115a and 121 of the Cat Co 3 beach section of the Pho Han Formation that corresponds to the expected location of the Hangenberg Crisis (Fig. II-4). While caution must be exercised when considering redox and productivity proxies, as many are inconsistent and controlled by lithology and/or depositional environment (Brumsack, 2006; Carmichael et al., 2016; Piper and Calvert, 2009; Tribovillard et al., 2006; Ver Straeten et al., 2011), the section studied has relatively consistent lithology (limestones, organic-rich limestones) with the exception of a minor increase in clay particles at the stratigraphic position of the Hangenberg Crisis. SEM-EDS analysis indicates that the only non-carbonate input is rare fine quartz silt and illite clay particles. Beds 116, 117, 120, and 121 (beds near the stratigraphic position of the D-C boundary) contain slightly more Al_2O_3 than the other samples, but SEM-EDS analysis of these beds reveals no change in mineralogy or mean grain size in these samples, only changes in the relative abundance of calcite, quartz silt, and illite clay. Additionally, microfacies analysis shows no major changes in depositional environment across the section (Komatsu et al., 2014). All bulk rock and trace elemental values (as well as detection limit) can be found in Table II-1.

4.1.1. Lithology and resulting caveats on proxy data

Although provenance analysis described by Bhatia and Crook (1986) is sometimes useful, the lack of significant sand-size detrital input from coastal margins (either active or passive) precludes this method. However, microfacies analysis is consistent with a carbonate basin setting that is far offshore (Komatsu et al., 2014).

Beds 116 and 117 at the expected location of the HBS event contain the most detrital material and are the most Al-rich samples in the section with an Al_2O_3 content of 2.9 wt. % compared to the average background value of 0.32 wt. % (for the Famennian part of the section). Extremely low Al content makes trace element normalization to Al quite problematic for interpreting redox and productivity proxies (Tribovillard et al., 2006), as minor changes in Al content will amplify natural scatter in trace element data rather than reflect actual excursions.

Average Al/Ti ratios in the Cat Co 3 section are 38.7 (Fig. II-5), more than double the average Al/Ti ratio of 17 found in the reference Post Archean Australian Shale (PAAS). This indicates Al scavenging by organic matter in the water column and/or diagenetic clay formation rather than a detrital contribution (Murray and Leinen, 1996). Furthermore, using the methodology of Van der Weijden (2002) that compares the coefficient of variation (the standard deviation divided by the mean) for Al against that of individual trace elements, nearly all the standard anoxia and productivity trace element proxies used in this study become distorted and potentially useless when normalized to Al. Taken together with the Al/Ti ratios, which indicate biological and/or diagenetic processes of Al deposition rather than detrital processes where normalization to shales would be useful, none of the geochemical proxy data used for this study has been normalized.

Previous studies show that changes from carbonate to clastic-dominated sedimentation can indicate total shutdown of the carbonate factory (Krencker et al., 2014). Carbonate factory demise is one mechanism that could have caused the change in sedimentation at beds 116 and 117 from carbonate-dominated lithologies to carbonates with slightly increased clay content and a high phosphorous accumulation rate (Krencker et al., 2014). As shown in Figure II-6, beds 116 and 117 contain the highest amounts of excess P_2O_5. The alternative explanation is that the clastic sediment had a

terrigenous/upslope/fluvial source. The Cat Co 3 section contains no increase in detrital proxies Ti/Al, Si/Al or Zr/Rb in beds 116 and 117. Therefore, we conclude that the change in lithology is due to a carbonate cycle perturbation, due to the lack of detrital (fluvial) sediments in beds 116 and 117.

4.1.2. Anoxia/Redox proxies

TOC enrichment is a primary indicator of oceanic anoxia (Calvert and Pedersen, 1992; Tribovillard et al., 2006), and the Pho Han Formation displays TOC enrichment between beds 115c and 120, with a maximum of 5.8 wt. % in bed 116 versus an average background value of <0.5 wt. % (Fig. II-4). Enrichments in total S are also used as a primary anoxia indicator (Lyons et al., 2003; Tribovillard et al., 2006). Beds 116 and 117 likewise show up to 2 wt. % S enrichment, which is likely controlled by the abundance of pyrite. Carbon isotope values do not show any noticeable trends throughout the section, even at the expected location of the Hangenberg Crisis, either in $\delta^{13}C$ in carbonate or in organic carbon (discrepancies in duplicate analyses are being investigated). This is not particularly unusual, especially within the South China block where $\delta^{13}C$ values across the Hangenberg Crisis interval are inconsistent (Bai et al., 1994; Qie et al., 2015). Although many studies do show a positive $\delta^{13}C$ excursion across the Hangenberg Crisis interval (reviewed in Kaiser et al., 2015), this excursion is not ubiquitous across all locations (Brand et al., 2004; Cramer et al., 2008; Kumpan et al., 2014a; Kumpan et al., 2014b). Therefore the absence of an obvious positive $\delta^{13}C$ excursion at the expected location of the Hangenberg Crisis does not negate the presence of the Hangenberg Crisis.

Authigenic U is rarely affected by detrital provenance (Tribovillard et al., 2006), and Pho Han sediments likewise show that authigenic U is not coupled with lithology (Fig. II-6). Authigenic U is distinguished from detrital U and calculated with the following formula: Uauth

35

= Utot –Th/3, where Th/3 approximates detrital uranium (Wignall and Myers, 1988). Bed 117 contains the largest amount of authigenic U (24.5 ppm), and surrounding beds 116-119 display elevated levels (>5 ppm).

Ce anomalies <-0.1 are generally considered to show anoxic signatures (German and Elderfield, 1990; Morad and Felitsyn, 2001; Wilde et al., 1996). Ce anomalies were calculated using the formula: Ceanom = log [3Cen/(2Lan + Ndn)], in which n signifies the REE normalization to the North American Shale Composite (NASC) (Elderfield and Greaves, 1982; Wright et al., 1987). Ce anomalies with La/Sm<0.35 indicate diagenetic apatite rather than ocean redox conditions (Morad and Felitsyn, 2001). La/Sm values within Pho Han sediments range between 4.07 and 12.01, indicating that Ce anomalies may be used to determine ocean redox conditions during deposition. Out of all geochemically sampled beds (104-126), only two beds (123 and 125) have Ce anomaly values that are not considered anoxic (Fig. II-6).

Mo accumulates in restricted basins under long-term anoxic conditions, with concentrations reaching 50-200 ppm (Algeo and Lyons, 2006; Algeo et al., 2007; Algeo and Maynard, 2008), and is rarely affected by detrital input (Tribovillard et al., 2006). Beds 116 and 117 showed a dramatic enrichment in Mo, with values 123 ppm and 44 ppm, respectively. Only five other beds (118, 119, 120, 121, and 124) contained Mo measurements that are above the detection limit (2 ppm), but none exceeded 10 ppm. Mo values of 0-20 ppm are correlated with non-euxinic conditions, 20-40 ppm to possible euxinia, 40-70 ppm to seasonal euxinia, and 70-90 ppm to possible well-established euxinia, and Mo values >90 ppm are diagnostic of persistent euxinic conditions (Formolo et al., 2014). However, Mo values can underestimate actual euxinic conditions due to Mo sequestration outpacing Mo resupply under sulfidic and euxinic conditions (Algeo, 2004). In these cases, additional proxies can be used, such as Mo/TOC ratios (Algeo and Lyons,

2006). The Mo > 90 ppm in Pho Han bed 116 and elevated values in bed 117 (44 ppm) indicate anoxic to highly euxinic conditions (Fig. II-4), consistent with the Hangenberg Crisis.

V ratios, such as V/Cr and V/(V+Ni), are also commonly used as redox proxies and have been used in a variety of studies. Other sections that cross the D-C boundary have shown dramatic increases in V/Cr at the Hangenberg Crisis (Beier and Hayes, 1989; Caplan and Bustin, 1998; Marynowski et al., 2012; Perkins et al., 2008; Rimmer, 2004). Early work by Ernst (1970) and Jones and Manning (1994) suggested that sedimentary V/Cr values >4.25 record anoxic conditions, 2.0-4.5 record dysoxic conditions, and <2.0 record fully oxic conditions. Hoffman et al. (1998) and Averbuch et al. (2005) countered that V/Cr = 1.0 is the dysoxic-anoxic boundary, and values 1-5 record anoxia. Modern euxinic environments including the Black Sea, the Cariaco Basin, the Saanich Inlet, and the Framvaren Fjord have V/Cr values ranging between 0.68 and 2.25 (calculated from Algeo and Maynard, 2004). The boundary between oxic and anoxic conditions as recorded by V/Cr ratios obviously varies with different studies, but in general increasing V/Cr ratios have been correlated with increased anoxia (e.g. Marynowski et al., 2012). Using the V/Cr criteria of Jones and Manning (1994) and Ernst (1970), most of the Cat Co Beach 3 section is oxic, with the exception of beds 109, 110, 111, 116, and 123 (Fig. II-6). Using the criteria of Hoffman et al. (1998), Averbuch et al. (2005), and Algeo and Maynard (2004), the entire section is anoxic.

In the case of the Pho Han Formation, V/(V+Ni) is possibly a better redox proxy than V/Cr because V and Ni are better preserved under anaerobic depositional conditions (Hatch and Leventhal, 1992). According to Hatch and Leventhal (1992), V/(V+Ni) ratios ≤0.46 represent oxic conditions, >0.46 and ≤0.60 represent dysoxic conditions, >0.54 and ≤0.82 represent suboxic to anoxic conditions, and >0.84 represents euxinia. All Pho Han beds have V/(V+Ni) values equal to or greater than 0.5., indicating prolonged dysoxia at a

37

minimum. A majority of the beds are suboxic to anoxic, and beds 104, 115a, 124, and 126 are considered euxinic.

Given the somewhat contradictory results from V ratios, concurrent enrichments in U, V, Mo, S and TOC may be better indicators of anoxia and euxinia. Correlated enrichments in these elements indicate euxinic conditions, because under reducing conditions these ions form insoluble precipitates or are adsorbed onto organic material (Hoffman et al., 1998; Tribovillard et al., 2006). This coupling is seen only in Pho Han beds 116-118 (Figs. II-4, II-5), which are within the expected Hangenberg interval. Co, Sb, and Tl can also be used as redox proxies (Brumsack, 2006; Piper and Calvert, 2009), but only Tl is not lithologically controlled. Beds 118-120 likewise display relative enrichments in Co and Sb, although trends are inconsistent (Fig. II-6). These proxies should be analyzed with caution and must be used alongside other methods like framboid analysis and PCA (see sections 4.2-4.3).

4.1.3. Productivity proxies

Phosphorous is commonly used as a paleoproductivity proxy to indicate increased biological productivity, necromass deposition, or secondary eutrophication (Middelburg and Levin, 2009; Schmitz et al., 1997; Tribovillard et al., 2006). In the beds from the Pho Han Formation, P_2O_5/Al_2O_3 increases within the expected Hangenberg interval, especially in beds 118 and 119 (Fig. II-7). Although Tribovillard et al. (2006) note that Ba enrichments are rarely affected by detrital provenance, anoxic depositional environments and the degree of sulfate reduction can lead to dissolution or undersaturation of barite (McKay and Pedersen, 2008). Furthermore, Ba can vary with water depth, and barite preservation can also vary with sedimentation rates (Dymond et al., 1992; McKay and Pedersen, 2008). Although excess Ba increases in the expected Hangenberg Crisis interval in the Pho Han sediments (Fig. II-7), it is probably an unreliable paleoproxy due to the prolonged suboxic/dysoxic

depositional environment. Nickel (Ni) and cadmium (Cd) can also be used as proxies for either anoxia or productivity (Brumsack, 2006; Tribovillard et al., 2006). When V/Ni ratios are >2.5, Ni enrichments indicate bottom water anoxia (Piper and Calvert, 2009), but only half of the analyzed Pho Han beds (beds 104-106, 108, 109, 112, 114, 115a, 118, 124-126) have V/Ni ratios >2.5. Cd and Ni are enriched within the expected Hangenberg Crisis interval within Pho Han sediments (Fig. II-7), but their enrichment mechanisms are unclear. Copper (Cu) and zinc (Zn) are micronutrients that are enriched during necromass deposition and usually included as solid solution phases in pyrite (Tribovillard et al., 2006). Both Cu and Zn are enriched within the expected Hangenberg Crisis interval within Pho Han sediments (Fig. II-7), indicating, along with other proxies, an increase in productivity between beds 115c and 121.

4.2. Principal component analysis

Due to the somewhat contradictory geochemical signals of some of the trace elements (particularly V, Cr, and Ni), principal component analysis (PCA) was used to clarify trace element enrichment and correlation between samples. PCA of major, minor, trace, and rare earth elements (Fig. II-8a) shows that the most variance is caused by mineralogy, with the largest variations in Si, Al, Fe, Mn, Ca, K, and Ti. Beds 115-117, 119-121, and 126 plot positive on the PCA 1 axis, indicating a lack of carbonate deposition. The rest of the beds are relatively enriched in Ca, indicating a carbonate-rich lithology, consistent with SEM-EDS observations. PCA of only trace elements reduced the influence of lithology in the analysis (Fig. II-8b). Positive values on the PCA 1 axis display relative enrichment in Mo, Cu, Ni, As, Co, Ce, La, excess SiO_2, and excess Ba. Samples that are positive on the PCA 1 axis are beds 113, 116-121, and 124, which is consistent with the expected location of the Hangenberg Event for beds 116-121. The PCA 2 axis has little redox/productivity

significance (most variation in rare earth elements rather than commonly-used redox proxies) and accounts for less geochemical variation than to PCA 1, so interpretations using this method are concentrated on PCA 1.

<u>*4.3 Framboidal pyrite*</u>

Circular aggregates of pyrite microcrysts (pyrite framboids) and their shape, size, and distribution can indicate varying degrees of dysoxia, anoxia, or euxinia in the water column (Wilkin et al., 1996). Framboids that formed in anoxic water columns tend to have a narrow size range, with individual framboids <5 μm in diameter, and are dispersed uniformly throughout the sediment rather than in large clumps or within burrows (Bond et al., 2004; Wang et al., 2013; Wignall and Newton, 1998; Wilkin and Barnes, 1997; Wilkin et al., 1996; Wilkin et al., 1997). Framboids in fluctuating dysoxic/oxic/anoxic/suboxic environments are typically larger and more variable in size, and less abundant (Wignall and Newton, 1998). A lack of framboids usually indicates oxic conditions, but can also be explained by euxinic depositional environments where the amount of available Fe is insufficient to form framboids (Wilkin and Barnes, 1997). Framboids that are found in burrows or pore spaces, as well as ovoid-shaped framboids that are >25 μm in diameter likely formed at or below the sediment-water interface and do not indicate water column anoxia (Carmichael et al., 2016; Rowan et al., 2009; Wang et al., 2013). Histogram shapes of the size distribution of framboids (Fig. II-9) also provide useful information about the degree of water column anoxia (Wignall and Newton, 1998).

Framboidal pyrite is abundant in all analyzed samples from the Cat Co Beach 3 section, and these framboids are generally very small (<10 μm). Eight representative samples (beds 104, 110, 115, 116, 117, 118, 121, 124, and 126) were analyzed in detail for pyrite framboid size distributions (Fig. II-10). Generally, framboid size is skewed to the right,

40

with most measured framboid diameters between 4 and 5 μm. Framboid sizes < 3.5 μm could not be accurately measured at the resolution used for the image processing and are not included in this analysis. Beds 116 and 117 have an order of magnitude more framboids than the surrounding beds, as shown by the first column of histograms in Figure II-9, which also explains their elevated sulfur content (Fig. II-4). The average framboid sizes in beds 116 and 117 are 4.56 μm and 4.26 μm, respectively, indicating deposition within anoxic to euxinic water conditions. Histogram shape comparisons between individual beds (Fig. II-10) and previous studies (Fig. II-9) suggest that the lower part of the section (beds 104, 110, and 115) ranges from intermittently dysoxic to upper dysoxic signatures, beds 116 and 117 match with anoxic to euxinic signatures, and the upper part of the section (beds 121, 124, and 126) matches with the upper dysoxic histogram shape.

All analyzed samples within beds 104-126 contain disseminated framboids, and the presence of even a small number of disseminated framboids reveals that the basin remained at least dysoxic throughout most of its history. This interpretation is consistent with redox proxies such as V/(V+Ni) and Ce anomalies that also show persistent, long-term dysoxic conditions within the basin. The exception to this is beds 116 and 117, which (regardless of proxy) exhibit highly anoxic to euxinic conditions, and are within the expected biostratigraphic location of the Hangenberg Crisis.

4.4 Hg chemostratigraphy

Mercury (Hg) chemostratigraphy can be useful for correlating sediments with volcanic events, as volcanism is the largest natural source of Hg, and Hg has a relatively long residence time in the atmosphere (0.5 - 2 years) that allows for wide distribution in the sedimentary record (Thibodeu et al., 2016; Bergquist, 2017; Charbonnier et al., 2017; Percival et al., 2017; Racki et al., 2018). Positive mercury anomalies have therefore been

linked to large-scale volcanism (Bergquist, 2017; Percival et al., 2017). Within the Pho Han sediments surrounding the D-C boundary, a marked Hg enrichment exceeding 1000 ppb is present that corresponds with the Hangenberg Event (Fig. II-4). As Hg can be correlated with organic matter rather than volcanic sources, Hg/TOC values were calculated as well (Table II-1). The interval of elevated Hg in the Pho Han Formation does correspond to some lithologies with higher organic content, but not all. Using the methodology of Racki et al. (2018), Hg/TOC anomalies exceeding 3x the median Hg/TOC values for the section are categorized as volcanic in source. These anomalies are present in beds 112 (3.2x the median) and 118 (23.6x the median) of the Pho Han Formation (Table II-2), suggesting that the source of Hg in those intervals is volcanic. Additional intervals (beds 116-118) also have elevated Hg/TOC values that correspond neatly with the Hangenberg Crisis and D-C transition. Very high or low TOC values can result in anomalously low/high Hg/TOC ratios, so caution must be exercised when interpreting this data. For this reason, Hg is also normalized to Al, Fe, and S.

To reduce the signature of potential detrital or local volcaniclastic source material, Hg/Al_2O_3 values were calculated (Table II-2) (see Fig. II-11 for Hg/Al), resulting in an excursion near the Hangenberg Crisis and D-C boundary interval. Due to low detrital influence, the Hg was probably sourced from atmospheric deposition. Hg was also normalized to Fe and S (to minimize effects of inclusion in pyrite), resulting in a similar excursion, particularly in bed 118 (Fig. II-11).

The most pronounced Hg anomaly is observed in bed 118, contrasting the strata recording the most severe anoxia and inferred Hangenberg Crisis (beds 116 and 117). A potential explanation is up-section migration via dissolution and reprecipitation reactions. This can occur when sediments deposited under anoxic conditions are overlain by sediments deposited under oxic conditions (Smit et al., 2016). This upward mobility of Hg

42

means that the potential volcanic activity and the Hangenberg Crisis may have occurred

concurrently. To further confirm the volcanic source, terrestrial sediments from the D-C

transition may be analyzed, which would be independent of ocean redox conditions and

marine Hg cycling (Percival et al., 2017), or Hg isotopes can be used (Thibodeau and

Bergquist, 2017).

5. Implications and Conclusions

       The Hangenberg Crisis has primarily been studied along active margins of large continental blocks of Laurussia and northern Gondwana, so it is important to determine in what ways the event is preserved in different paleogeographic locations. Using a multi-proxy approach, this study shows that the Hangenberg Crisis can be more narrowly constrained within a section with relatively limited biostratigraphic control. Although anoxia and productivity proxies are not always reliable, they are useful for identifying anoxia events when used in conjunction with PCA and pyrite framboid distributions. In the Pho Han Formation, the basin was not fully oxygenated even before and after the Hangenberg Crisis. During the Hangenberg Crisis (which likely represents a total shutdown of the carbonate factory), the normally dysoxic to anoxic water column likely became euxinic.

       Hg enrichment at/near the Hangenberg Crisis interval suggests that the trigger mechanism for the Hangenberg Crisis and the associated D-C boundary extinction event may have been widespread volcanic activity. Additional Hg isotope data will be helpful in confirming the source of the Hg, but as there is no local source of Hg for these sediments, the presence of Hg anomalies in a sediment-starved, passive margin carbonate basin is particularly notable. Although there is no single LIP that is associated with the Hangenberg Crisis (Bond and Wignall, 2014), the recent work by Racki et al. (2018) suggests the Hg anomalies at the Frasnian-Famennian boundary were due to widespread arc volcanism associated with the Appalachian/Variscan orogeny rather than a LIP event. As this orogenic event was ongoing throughout the Devonian and Carboniferous, it seems reasonable to explore the possibility that the Hangenberg Crisis was also triggered by similarly intensive arc volcanism.

Tables: Table II-1. Values of all bulk and trace elements measured in this study. Sample names begin with "VN-."

Analyte Symbol	SiO$_2$	Al$_2$O$_3$	Fe$_2$O$_3$(T)	MnO	MgO	CaO	Na$_2$O	K$_2$O	TiO$_2$	P$_2$O$_5$	LOI	Total	Mass
Unit Symbol	%	%	%	%	%	%	%	%	%	%	%	%	g
Detection Limit	0.01	0.01	0.01	0.001	0.01	0.01	0.01	0.01	0.001	0.01		0.01	
VN-104	1.07	0.37	0.29	0.107	0.63	53.78	0.07	0.09	0.016	0.03	42.84	99.31	1.185
VN-105	0.85	0.26	0.25	0.08	0.72	55.41	0.08	0.04	0.004	0.03	41.32	99.04	1.346
VN-106	0.86	0.3	0.21	0.073	0.74	54.41	0.07	0.06	0.005	0.04	42.66	99.44	1.214
VN-108	0.71	0.18	0.13	0.093	0.67	54.2	0.06	0.03	0.002	0.04	43.03	99.13	1.451
VN-109	0.75	0.16	0.15	0.084	0.61	55.27	0.05	0.03	0.003	0.02	43.12	100.2	1.359
VN-110	0.61	0.13	0.12	0.148	0.6	55.11	0.04	0.03	0.004	0.03	43.16	99.99	1.383
VN-111	0.86	0.19	0.27	0.142	0.67	55.08	0.07	0.03	0.003	0.04	42.76	100.1	1.479
VN-112	0.89	0.25	0.2	0.067	0.59	54.2	0.03	0.05	0.006	0.04	43.28	99.6	1.035
VN-113	1.55	0.68	0.43	0.076	1.65	52.99	0.05	0.15	0.018	0.04	42.91	100.5	1.446
VN-114	0.96	0.25	0.22	0.102	1.2	53.35	0.04	0.06	0.006	0.04	42.79	99.02	1.503
VN-115	2.05	0.89	0.33	0.047	0.76	52.09	0.36	0.17	0.041	0.03	42.29	99.07	0.779
VN-115A	0.67	0.17	0.17	0.075	0.62	54.84	0.04	0.03	0.005	0.03	43.45	100.1	0.947
VN-116	5.86	2.29	2.06	0.025	0.9	45.13	0.13	0.58	0.127	0.19	41.36	98.66	0.5841
VN-117	5.3	1.91	1.73	0.029	0.9	47.82	0.41	0.48	0.057	0.38	39.5	98.52	0.7092
VN-118	0.86	0.2	0.26	0.026	0.81	54.23	0.05	0.04	0.004	0.09	42.64	99.21	1.4
VN-119	1.14	0.42	0.42	0.027	0.79	53.96	0.04	0.1	0.015	0.13	42.46	99.49	1.459
VN-120	2.63	1.01	0.6	0.027	0.62	52.08	0.06	0.25	0.045	0.07	42.32	99.71	1.249
VN-121	5.24	1.58	0.86	0.028	0.69	49.97	0.04	0.42	0.067	0.04	40.2	99.14	1.387
VN-122	1.475	0.48	0.54	0.052	0.64	53.445	0.095	0.12	0.021	0.05	42.54	78.19	0.7825
VN-123	1.26	0.23	0.21	0.046	0.65	54.34	0.04	0.06	0.006	0.03	42.9	99.77	1.375
VN-124	1.65	0.45	0.16	0.033	0.55	53.9	0.07	0.1	0.006	0.04	42.53	99.5	1.357
VN-125	1.34	0.24	0.18	0.036	0.59	54.92	0.03	0.06	0.006	0.03	42.77	100.2	1.445
VN-126	2.345	0.805	0.205	0.028	0.58	52.965	0.215	0.185	0.011	0.095	42.34	99.775	0.87695

Analyte Symbol	Au	Ag	As	Ba	Br	Cd	Co	Cr	Cs	Cu	Hg	In	Ir	Mo	Ni
Unit Symbol	ppb	ppm	ppm	ppm	ppm	ppm	ppm	ppm	ppm	ppm	ppm	ppm	ppb	ppm	ppm
Detection Limit	1	0.5	1	1	0.5	0.5	0.1	0.5	0.1	1	1	0.1	1	2	1
VN-104	< 1	< 0.5	3	7	< 0.5	< 0.5	1	14.8	< 0.2	13	< 1		< 1	< 2	4
VN-105	4	< 0.5	1	7	< 0.5	< 0.5	< 0.1	6.1	0.3	4	< 1	< 0.1	< 1	< 2	5
VN-106	< 1	< 0.5	3	8	< 0.5	0.6	1.2	13.7	0.3	6	< 1	< 0.1	< 1	< 2	6
VN-108	2	< 0.5	2	6	0.9	0.7	< 0.1	3.8	0.2	6	< 1	< 0.1	< 1	< 2	4
VN-109	< 1	< 0.5	2	6	< 0.5	< 0.5	< 0.1	1.9	0.3	2	< 1	< 0.1	< 1	< 2	4
VN-110	< 1	< 0.5	1	6	0.5	< 0.5	0.9	1.3	0.3	3	< 1	< 0.1	< 1	< 2	5
VN-111	< 1	< 0.5	3	7	0.9	< 0.5	1.1	1.7	0.3	10	< 1	< 0.1	< 1	< 2	7
VN-112	< 1	< 0.5	1	7	1.2	< 0.5	0.9	< 0.5	< 0.2	2	< 1		< 1	< 2	5
VN-113	< 1	< 0.5	5	10	1	1	3.8	15.3	0.5	13	< 1	< 0.1	< 1	< 2	21
VN-114	< 1	< 0.5	3	7	< 0.5	< 0.5	1.1	4.5	0.3	7	< 1	< 0.1	< 1	< 2	6
VN-115	< 1	< 0.5	2	7	0.8	< 0.5	0.8	7	< 0.2	7	< 1		8	< 2	7
VN-115A	< 1	< 0.5	2	5	1.2	< 0.5	< 0.1	5	< 0.2	2	< 1		< 1	< 2	2
VN-116	29	< 0.5	17	22	7.3	1.7	8.6	23	< 0.2	48	< 1		29	123	58
VN-117	3	< 0.5	17	18	6.2	0.8	7.8	13.2	< 0.2	47	< 1		3	44	32
VN-118	3	< 0.5	2	7	2.1	< 0.5	0.8	3.9	0.3	10	< 1	< 0.1	< 1	4	5
VN-119	< 1	< 0.5	6	9	1.1	0.6	2.4	7.8	0.4	14	< 1	< 0.1	< 1	9	14
VN-120	9	< 0.5	8	13	< 0.5	0.8	3.5	17.9	0.7	22	< 1	< 0.1	< 1	3	33
VN-121	< 1	< 0.5	10	18	1.3	0.6	6.3	23.2	1.1	25	< 1	< 0.1	< 1	5	35
VN-122	15.5	< 0.5	3.5	7.5	2.15	< 0.5	3.6	4.1	< 0.2	7.5	< 1		< 1	< 2	6
VN-123	< 1	< 0.5	3	7	1.6	< 0.5	1.5	1.7	0.3	3	< 1	< 0.1	< 1	< 2	6
VN-124	3	< 0.5	3	8	1.3	< 0.5	< 0.1	6	0.5	3	< 1	< 0.1	< 1	3	5
VN-125	< 1	< 0.5	2	7	0.9	< 0.5	1.2	4.5	0.3	3	< 1	< 0.1	< 1	< 2	4
VN-126	< 1	< 0.5	1.5	7	1.65	< 0.5	1.55	10.25	< 0.2	3.5	< 1		12.5	< 2	3.5

Analyte Symbol	Pb	Rb	S	Sb	Sc	Se	Sn	Ta	U	W	Y	Zn	Zr	Ce	Pr
Unit Symbol	ppm	ppm	%	ppm	ppm	ppm	ppm	ppm	ppm	ppm	ppm	ppm	ppm	ppm	ppm
Detection Limit	5	1	0.001	0.1	0.01	0.5	1	0.01	0.01	1	1	1	1	0.05	0.01
VN-104	< 5	< 10	0.068	0.4	1.42	< 0.5		< 0.3	1.1	< 1	23	20	8	14	
VN-105	< 5	2	0.039	0.3	3.2	< 0.5	< 1	0.27	1.6	< 1	21	13	4	27.3	5.09
VN-106	< 5	2	0.085	0.2	4	< 0.5	< 1	0.3	0.89	< 1	15	10	4	8.25	2.04
VN-108	< 5	1	0.032	0.1	0.64	< 0.5	1	0.27	0.74	< 1	9	39	4	4.54	0.97
VN-109	< 5	1	0.038	0.2	0.43	< 0.5	< 1	0.3	0.8	< 1	9	11	4	4.47	0.99
VN-110	< 5	1	0.053	0.3	0.58	< 0.5	< 1	0.29	0.64	< 1	11	12	3	6.86	1.43
VN-111	< 5	1	0.098	0.3	0.46	< 0.5	< 1	0.25	0.85	< 1	7	46	4	4.41	0.83
VN-112	< 5	< 10	0.071	0.1	1.22	< 0.5		< 0.3	1.4	< 1	19	33	5	8	
VN-113	< 5	5	0.119	0.6	2.37	< 0.5	< 1	0.27	1.51	< 1	18	34	6	12.6	2.85
VN-114	< 5	2	0.164	0.4	0.87	< 0.5	< 1	0.35	1.07	< 1	8	13	4	5.11	1.19
VN-115	< 5	< 10	0.077	0.3	0.45	< 0.5		< 0.3	3.3	7	9	9	191	8	
VN-115A	< 5	< 10	0.029	0.1	0.53	< 0.5		< 0.3	1.4	< 1	13	7	7	4	
VN-116	10	10	1.43	1.1	2.3	< 0.5		< 0.3	21	4	23	72	81	42	
VN-117	< 5	< 10	1.62	0.8	1.75	< 0.5		< 0.3	29	1	27	39	66	43	
VN-118	< 5	2	0.18	0.3	0.51	< 0.5	< 1	0.3	8.37	< 1	8	17	4	9.68	1.21
VN-119	< 5	3	0.344	0.7	0.92	< 0.5	< 1	0.3	7.09	< 1	12	23	7	14.6	2.34
VN-120	< 5	8	0.374	0.9	2.46	< 0.5	< 1	0.34	4	< 1	18	47	17	15.3	2.87
VN-121	8	15	0.648	1.3	2.51	< 0.5	< 1	0.38	4.57	< 1	16	42	16	21.1	3.23
VN-122	< 5	< 10	0.129	0.3	0.67	< 0.5			3.95	2	10.5	10	33	8	
VN-123	< 5	2	0.092	0.1	0.47	< 0.5	< 1	0.3	2.17	< 1	6	7	4	8.45	1.02
VN-124	< 5	4	0.08	0.3	1.54	< 0.5	5	0.22	2.76	< 1	14	11	9	29.3	7.92
VN-125	< 5	2	0.073	0.2	0.71	< 0.5	< 1	0.29	2.73	< 1	8	9	3	12	1.39
VN-126	< 5	< 10	0.0505	0.2	1.26	< 0.5		< 0.3	3.6	1	16.5	10.5	27	20	

Analyte Symbol	Gd	Dy	Tl	Be	V	Ga	Ge	Sr	Nb	La	Nd	Sm	Eu	Tb
Unit Symbol	ppm	ppm	ppm	ppm	ppm	ppm	ppm	ppm	ppm	ppm	ppm	ppm	ppm	ppm
Detection Limit	0.01	0.01	0.05	1	5	1	0.5	2	0.2	0.05	0.05	0.01	0.005	0.01
VN-104				< 1	21			272		15.4	17	2.44	0.6	0.3
VN-105	3.84	3.23	0.07	< 1	23	1	< 0.5	284	0.8	22.7	21.1	4.25	1.01	0.56
VN-106	2.21	1.83	0.07	< 1	23	1	< 0.5	309	0.6	8.95	8.47	2.2	0.5	0.31
VN-108	0.96	0.98	< 0.05	< 1	12	1	< 0.5	266	0.4	6.34	4.13	0.94	0.23	0.16
VN-109	1	0.85	< 0.05	< 1	11	1	< 0.5	314	0.4	6.08	4.65	0.96	0.224	0.15
VN-110	1.46	1.25	0.06	< 1	10	1	< 0.5	296	0.4	7.82	6.07	1.24	0.33	0.22
VN-111	0.82	0.79	0.06	< 1	17	1	< 0.5	285	0.3	4.86	3.71	0.78	0.204	0.13
VN-112				< 1	14			295		9.24	6	1.51	0.4	0.2
VN-113	2.89	2.47	0.07	< 1	21	2	0.5	305	0.5	13.6	12.4	2.87	0.652	0.43
VN-114	1.07	1.12	0.08	< 1	17	1	< 0.5	351	0.6	5.57	4.95	1.21	0.317	0.19
VN-115				< 1	7			334		8.07	8	0.75	0.3	< 0.1
VN-115A				< 1	15			286		5.23	2	0.68	< 0.2	< 0.1
VN-116				< 1	116			545		33.2	24	3.65	0.8	0.3
VN-117				< 1	41			578		36	27	3.75	0.9	0.5
VN-118	0.8	0.75	0.22	< 1	14	< 1	< 0.5	508	0.2	9.73	4.55	0.81	0.194	0.12
VN-119	1.63	1.37	0.46	< 1	19	1	< 0.5	515	0.4	15.6	9.5	1.7	0.336	0.24
VN-120	2.18	2.13	0.28	< 1	50	2	< 0.5	437	1	17.3	11.3	2.02	0.448	0.34
VN-121	2.44	2.15	0.31	< 1	64	3	< 0.5	357	1.7	17.1	12.3	2.68	0.604	0.36
VN-122				< 1	11.5			269.5		5.665	2.5	0.885	0.1	< 0.1
VN-123	0.86	0.75	0.11	< 1	11	< 1	< 0.5	294	0.3	4.8	4.19	1	0.216	0.13
VN-124	9.66	13.3	0.08	< 1	28	1	0.6	358	0.6	31.8	34.5	7.07	0.895	1.82
VN-125	1.1	0.97	0.06	< 1	16	< 1	< 0.5	245	< 0.2	7.15	5.33	1.17	0.275	0.17
VN-126				< 1	21			310.5		11.7	14	2.22	0.45	0.4

Analyte Symbol	Ho	Er	Tm	Yb	Lu	Hf	Bi	Th
Unit Symbol	ppm	ppm	ppm	ppm	ppm	ppm	ppm	ppm
Detection Limit	0.01	0.01	0.005	0.01	0.002	0.1	0.1	0.05
VN-104				1.01	0.2	< 0.2	< 2	0.6
VN-105	0.61	1.71	0.242	1.44	0.211	0.2	< 0.1	1.64
VN-106	0.36	1.03	0.146	0.88	0.127	0.2	< 0.1	0.35
VN-108	0.19	0.53	0.082	0.53	0.072	0.2	< 0.1	0.14
VN-109	0.17	0.52	0.075	0.46	0.073	0.1	< 0.1	0.14
VN-110	0.26	0.73	0.095	0.53	0.075	0.2	< 0.1	0.18
VN-111	0.15	0.43	0.064	0.39	0.057	0.2	< 0.1	0.14
VN-112				0.7	0.12	< 0.2	< 2	0.6
VN-113	0.46	1.28	0.175	0.98	0.141	0.2	< 0.1	0.65
VN-114	0.21	0.55	0.078	0.5	0.081	0.1	< 0.1	0.36
VN-115				0.65	0.05	5.5	< 2	1.2
VN-115A				0.38	0.09	< 0.2	< 2	< 0.1
VN-116				1.55	< 0.01	1.8	< 2	3.5
VN-117				1.55	0.03	1.4	< 2	1.5
VN-118	0.15	0.48	0.076	0.51	0.07	0.2	< 0.1	0.21
VN-119	0.27	0.77	0.116	0.71	0.103	0.3	< 0.1	0.46
VN-120	0.43	1.26	0.189	1.21	0.192	0.5	< 0.1	1.19
VN-121	0.42	1.24	0.176	1.12	0.164	0.6	< 0.1	2.19
VN-122				0.65	0.08	0.75	< 2	0.7
VN-123	0.14	0.39	0.057	0.37	0.058	0.2	< 0.1	0.27
VN-124	3.18	9.46	1.21	7.14	1.04	0.4	0.3	1.46
VN-125	0.19	0.54	0.08	0.5	0.075	< 0.1	< 0.1	0.25
VN-126				0.83	0.07	0.6	< 2	0.65

Table II-2. Hg, TOC, Al_2O_3, Mo data as well as Hg/TOC and Hg/Al_2O_3 ratios from the Pho Han Formation, using the methodology of Racki et al. (2018). NA = Hg not analyzed. Gray shading represents incalculable data. Green shading represents data points that are greater than three times the median value. Yellow shading represents elevated Hg values above the median (but less than three times the median value). The median value of Hg/TOC is 66, and the median value of Hg/Al_2O_3 is 67.

Sample	Hg (ppb)	TOC (%)	Al_2O_3 (%)	Mo (ppm)	Hg/TOC	Hg/Al_2O_3
VN06-104	18	0	0.37	4	TOC = 0	49
VN06-2014-105	20	0.2	0.26	5	100	77
VN06-2014-106	14	0	0.30	6	TOC = 0	47
VN06-2014-108	NA	0	0.18	4	NA	NA
VN06-2014-109	NA	0	0.16	4	NA	NA
VN06-2014-110	NA	0.5	0.13	5	NA	NA
VN06-2014-111	NA	0	0.19	7	NA	NA
VN06-112	21	0.1	0.25	5	210	84
VN06-2014-113	18	0.1	0.68	21	180	26
VN06-2014-114	36	0	0.25	6	TOC = 0	144
VN-115	19	0	0.89	7	TOC = 0	21
VN06-115A	10	0.5	0.17	2	20	59
VN-116	548	5.3	2.29	58	103	239
VN-117	649	5.8	1.91	32	112	340
VN06-2014-118	1090	0.7	0.20	5	1557	5450
VN06-2014-119	372	4.1	0.42	14	91	886
VN06-2014-120	132	2	1.01	33	66	131
VN06-2014-121	30	0.8	1.58	35	40	19
VN06-122	51	4.5	0.48	6	11	106
VN06-2014-123	11	3.5	0.23	6	3	48
VN06-2014-124	15	0.7	0.45	5	21	33
VN06-2014-125	16	0.9	0.24	4	18	67
VN06-126	13	0.2	0.81	3.5	65	16
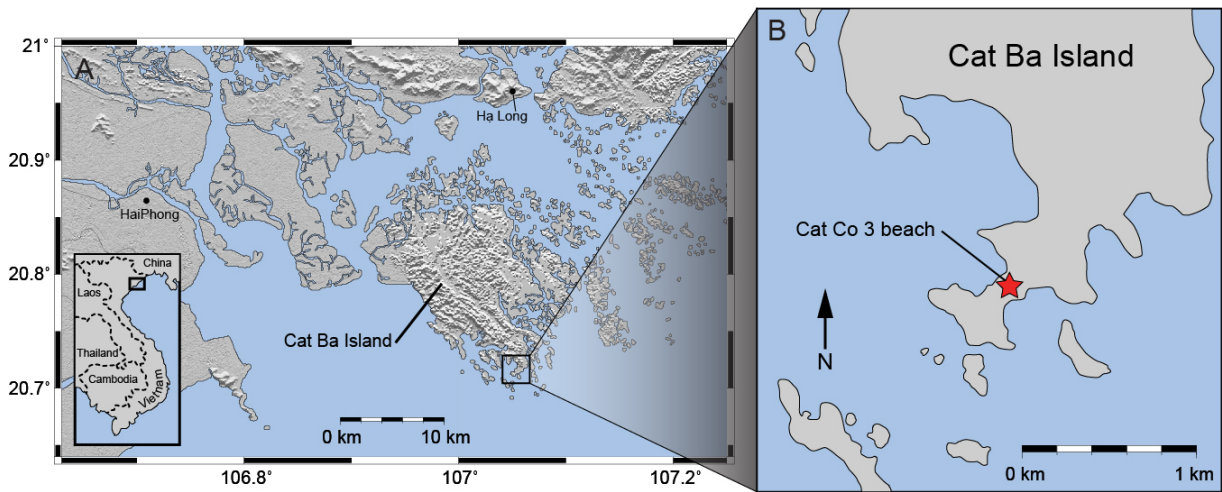
Figure II-1. (A) Cat Ba Island in northern Vietnam. (B) Study location at Cat Co 3 beach (N 20° 42'58, 0", E 107° 02'54, 8") on southern part of Cat Ba Island. Figure modified from Komatsu et al. (2014).
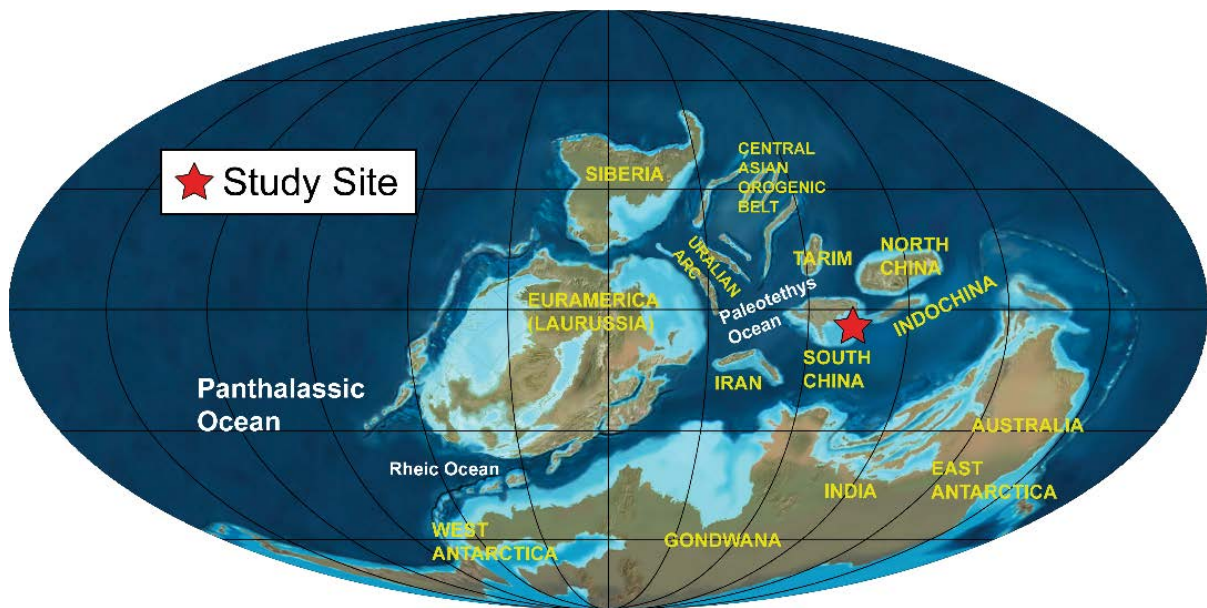
Figure II-2. Paleogeographic reconstruction of the continents during the Late Devonian with this study's location in red. Figure modified from Blakey (2016), using updated paleogeographic data for Asia from Xiao et al. (2010) and Metcalfe (2009).
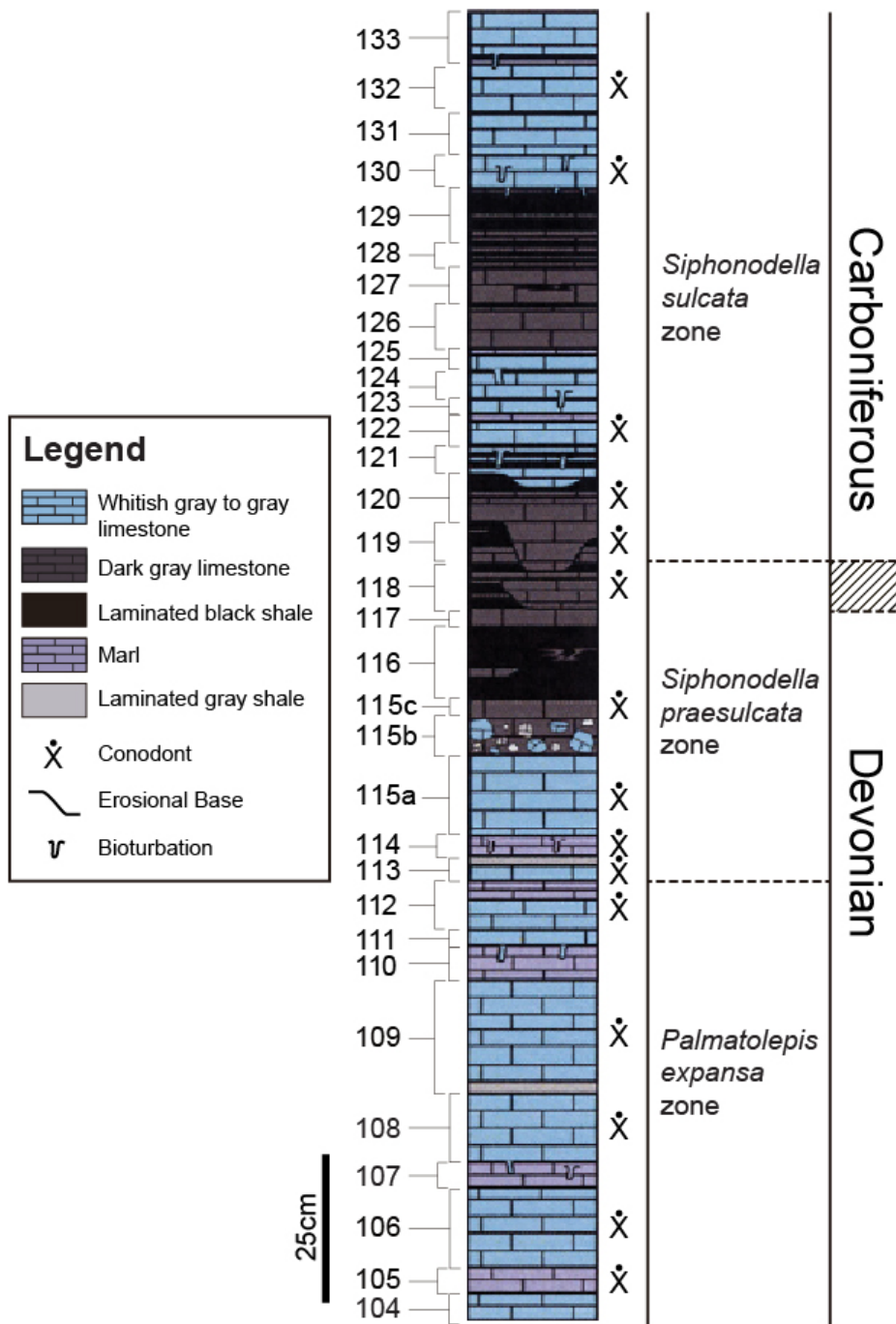
Figure II-3. Stratigraphic column as defined in Komatsu et al. (2014). Using conodont biostratigraphy, the most probable location of the D-C transition is within beds 117-118. Uncertainty in the conodont biostratigraphic record, as described by Corradini et al. (2011), requires that the D-C transition is a zone (shown by hatchmarks) rather than a sharp boundary.
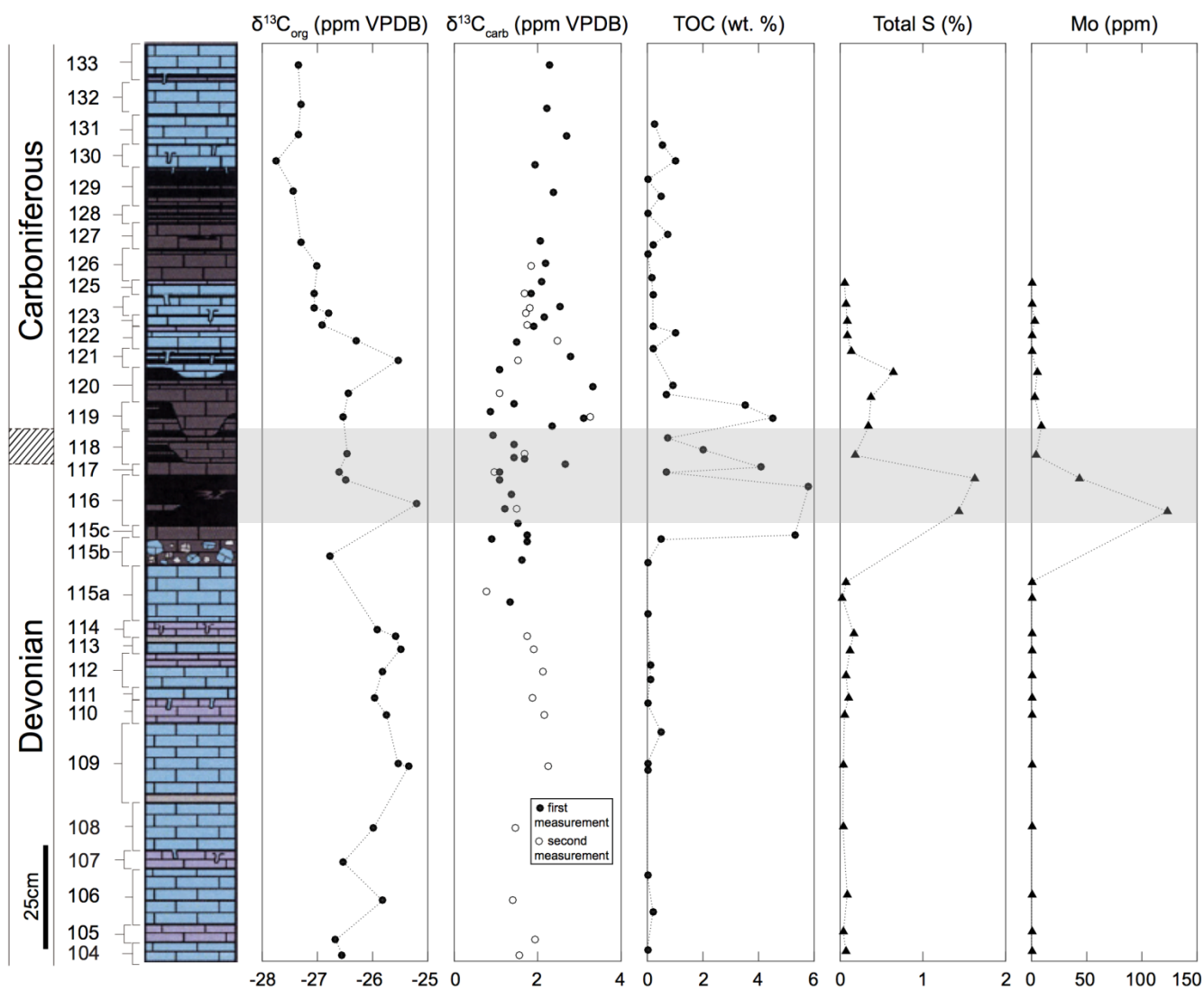
Figure II-4. Chemostratigraphy plots of carbon, including total organic carbon (TOC), total S, and Mo. TOC, total S, and Mo show enrichments immediately below the D-C boundary, in the expected location of the Hangenberg Crisis (beds 116-118, shaded).
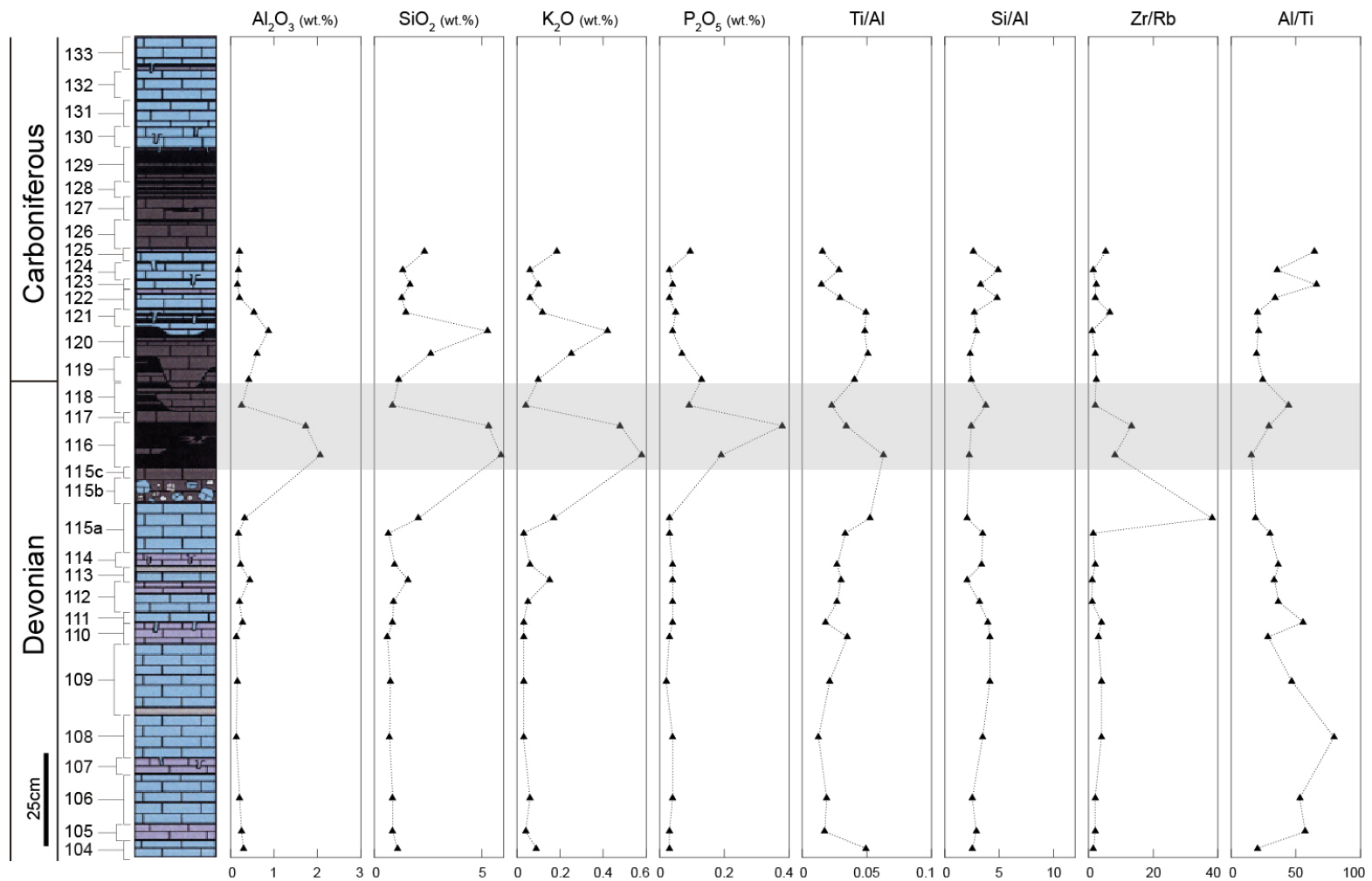
Figure II-5: Chemostratigraphy plots of lithologic proxies (Al_2O_3, SiO_2, K_2O, Ti/Al, Si/Al, Zr/Rb, and Al/Ti). The expected location of the Hangenberg Crisis (beds 116-118) is shaded.
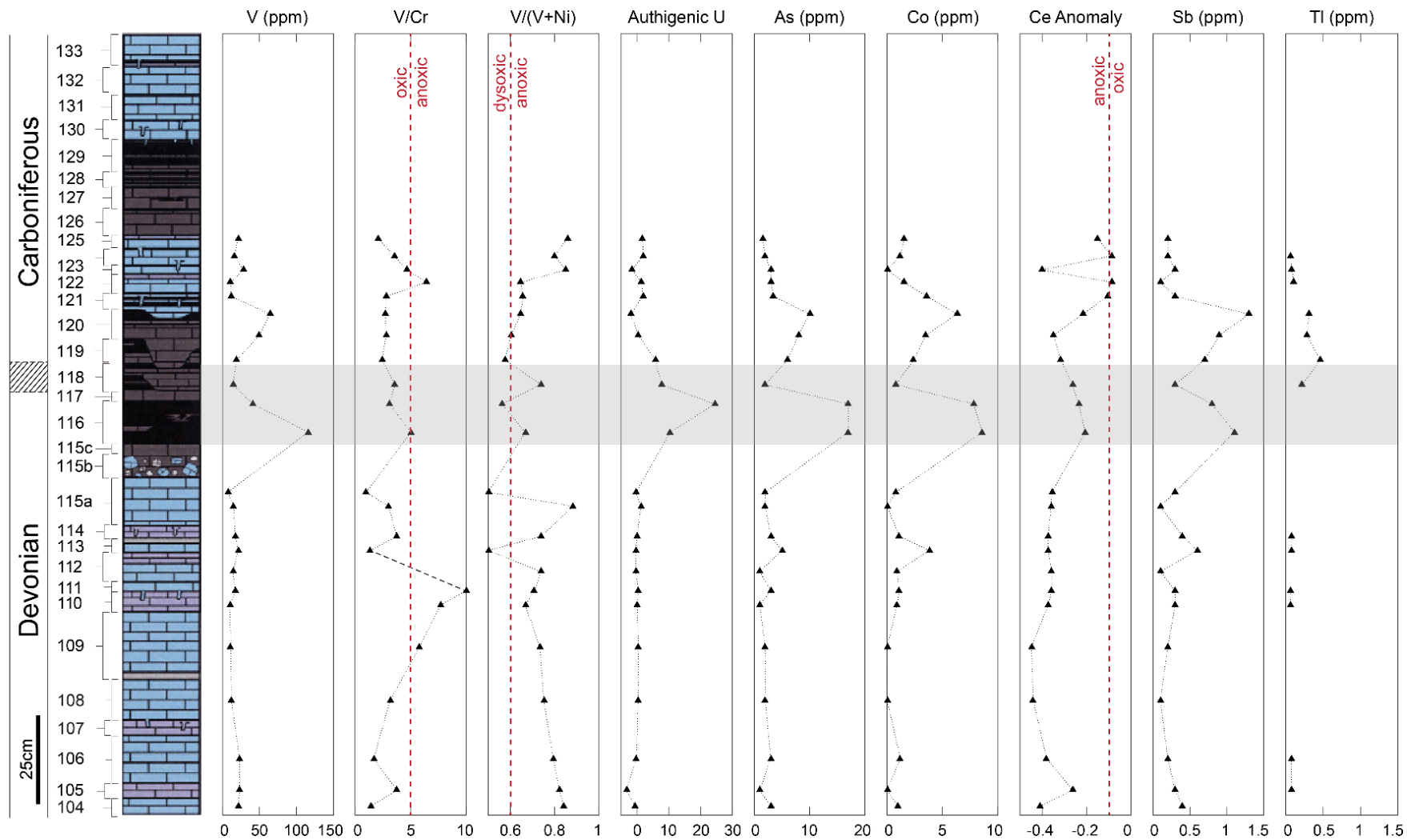
Figure II-6. Chemostratigraphy plots of common redox proxies. Dashed red lines represent anoxic values of proxies. A Ce anomaly <-0.1 is considered anoxic, according to Wilde et al. (1996) and Morad and Felitsyn (2001). V/Cr>5 and V/(V+Ni)>0.6 is anoxic according to Hoffman et al. (1998). Beds 116-118 are shaded, representing the Hangbenberg Crisis interval.
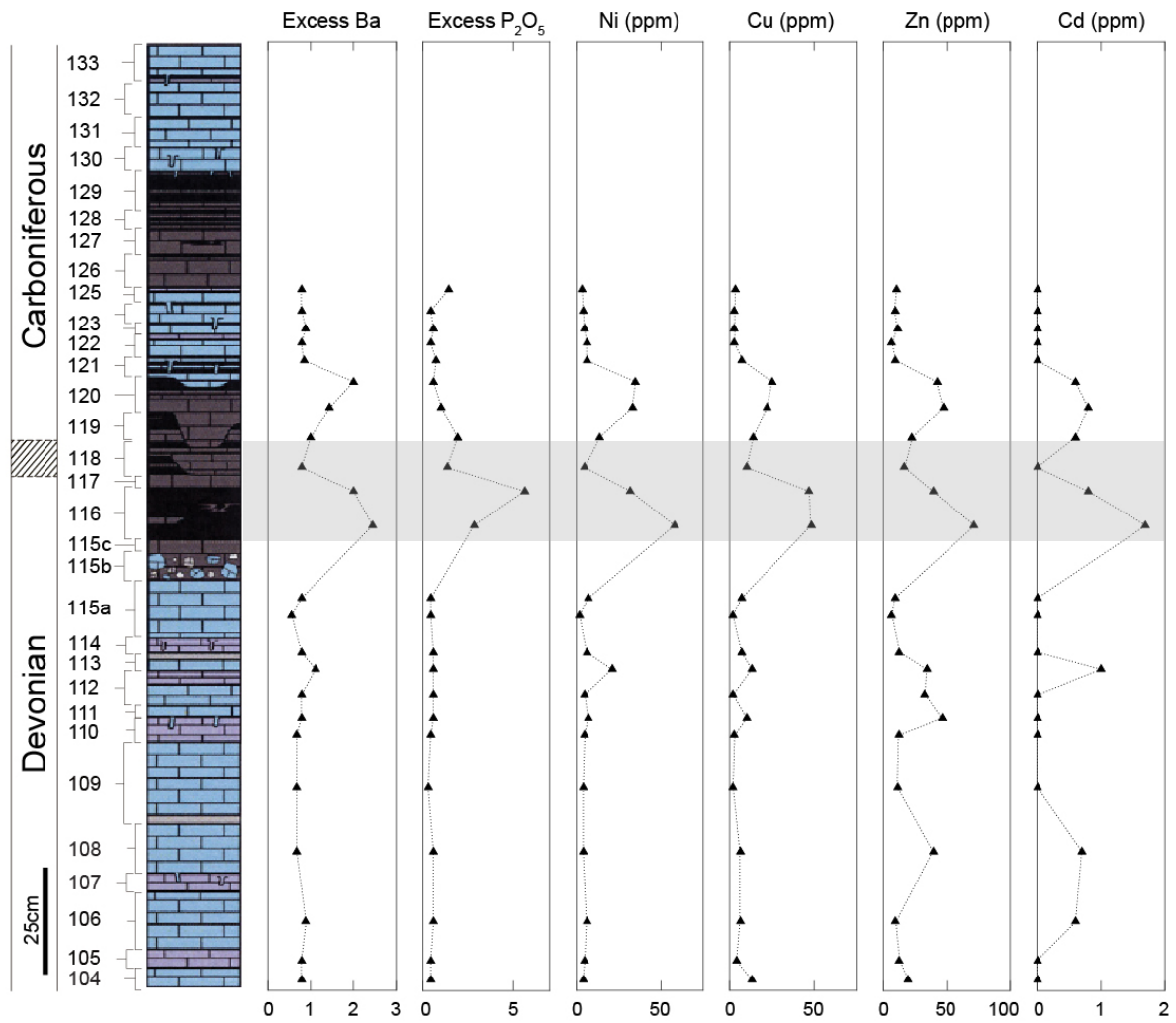
Figure II-7. Chemostratigraphy plots of common productivity proxies, all of which display relative enrichments below the D-C boundary, at the expected location of the Hangenberg Event. Beds 116-118 are shaded, representing the Hangbenberg Crisis interval.
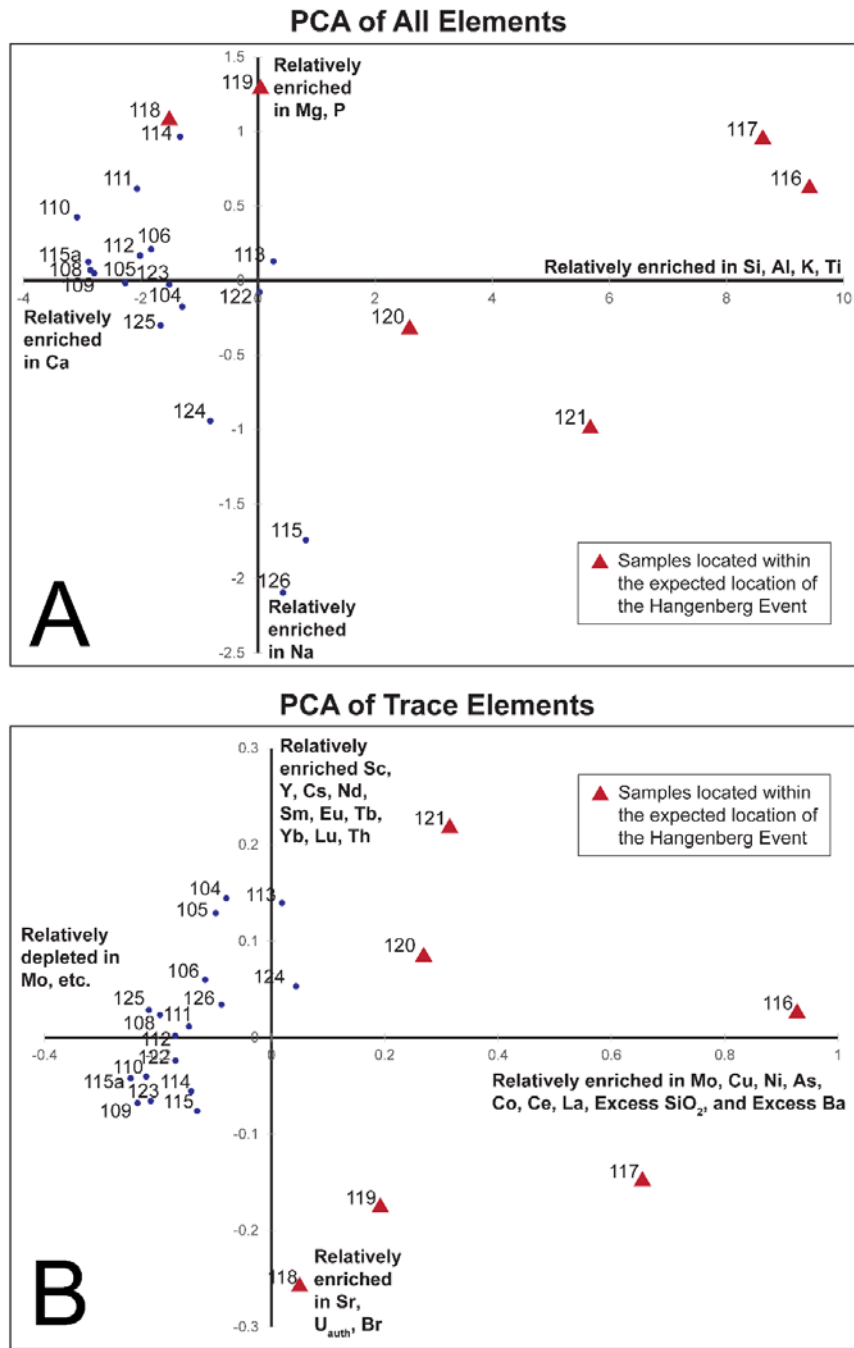
Figure II-8: (A) Principal component analysis (PCA) of all elements, including major and trace elements. The major elements account for the most variation within all samples (Si, Al, K, Ti, and Ca). The red triangles represent beds that are near the expected location of the Hangenberg Crisis. (B) PCA of trace elements (all major elements removed from analysis). The beds surrounding the expected location of the Hangenberg Crisis are relatively enriched in Mo, Cu, Ni, As, Co, Ce, La, excess SiO_2, and excess Ba, most of which are indicative of anoxic depositional environments or increased productivity.
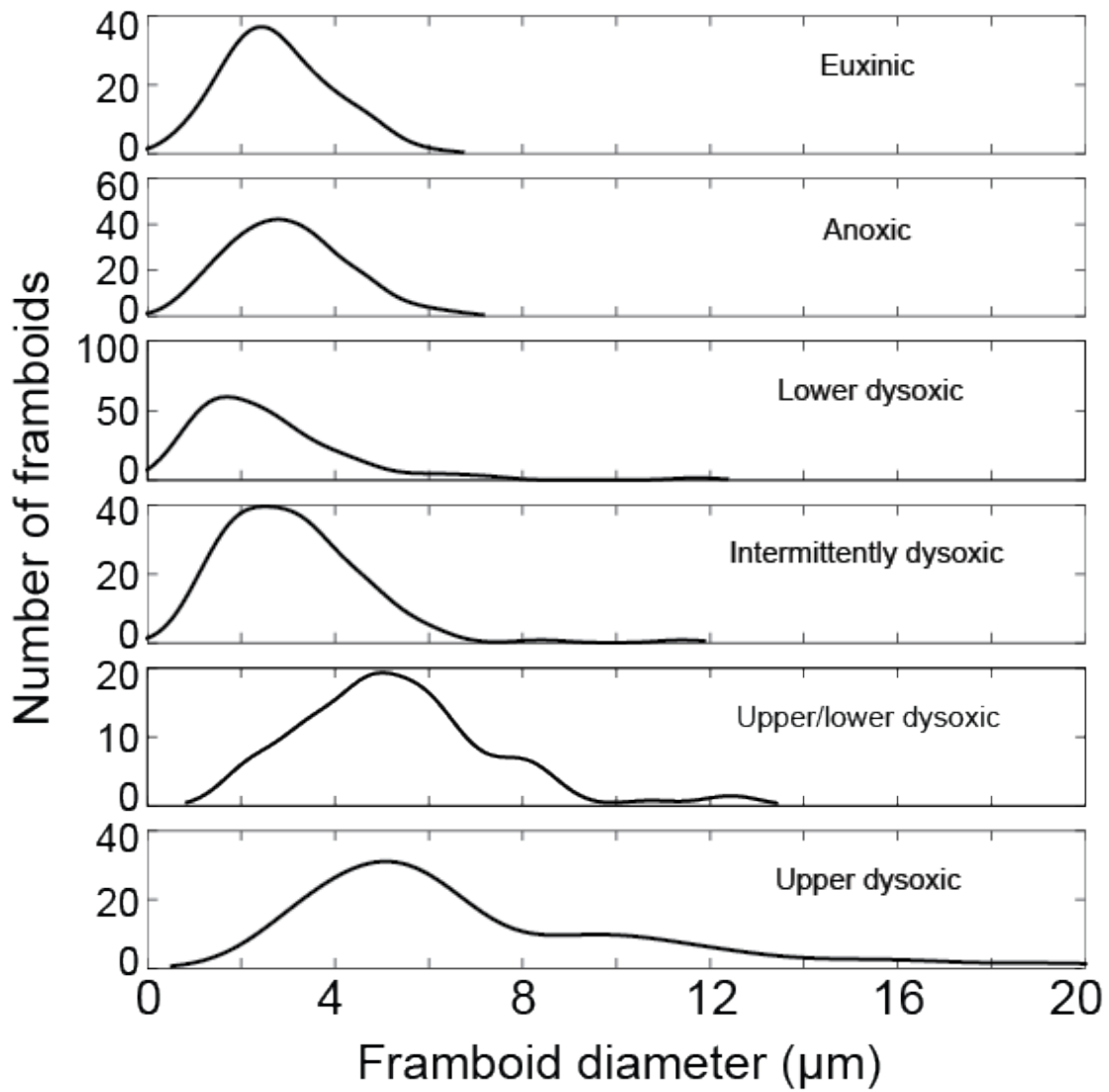
Figure II-9. Size distributions of framboids from depositional environments with variable degrees of anoxia. Histogram density functions were computed using the kernel distribution fit in MATLAB. Data from Wignall and Newton (1998).
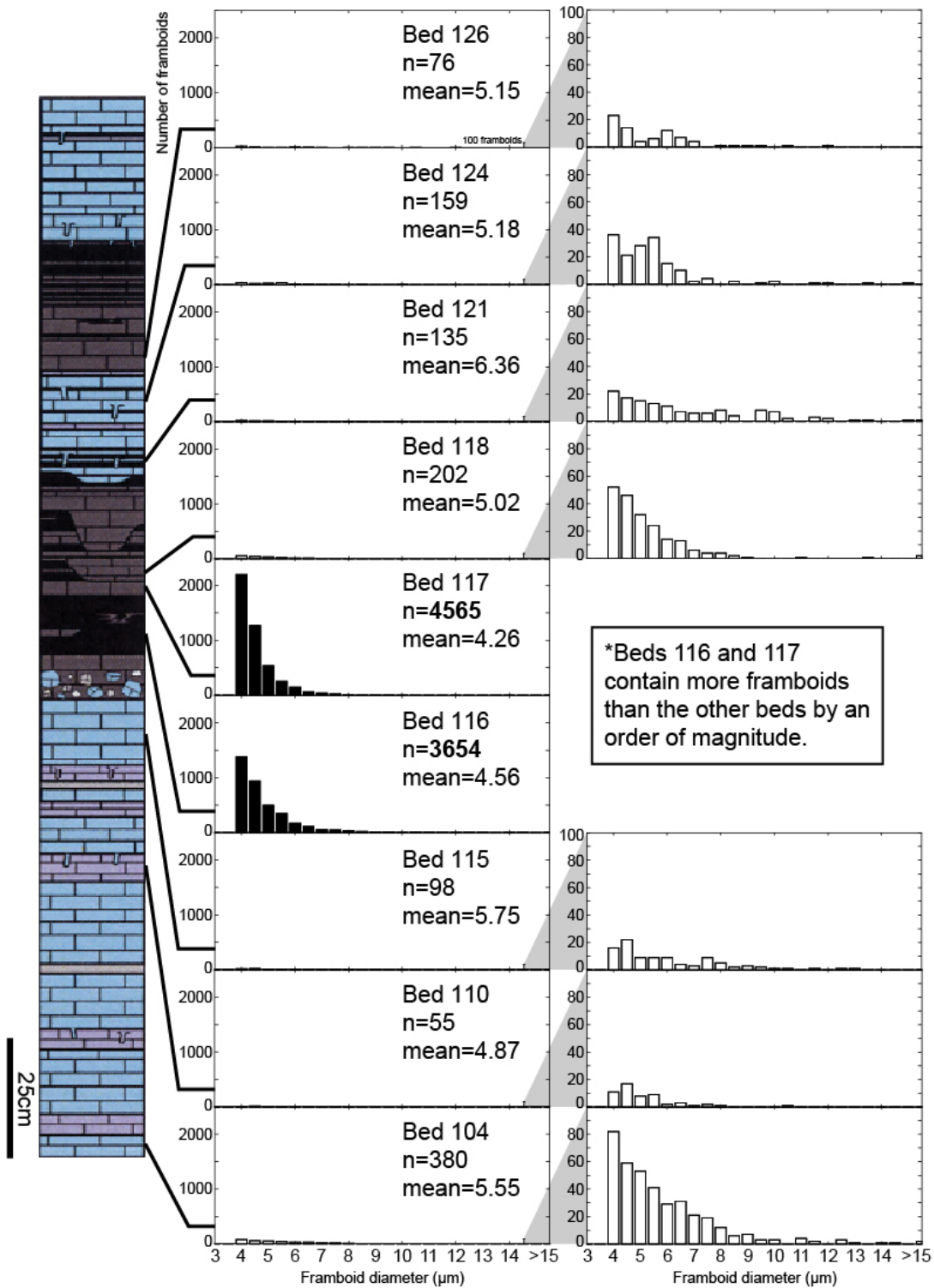
Figure II-10. Abundance and size distribution of pyrite framboids in representative samples throughout the section. Framboid diameter bin size for histograms is 0.5 µm. Graphs on the left represent framboid distributions for all beds; graphs on the right represent framboid distributions for beds with >1000 framboids per cm^2.
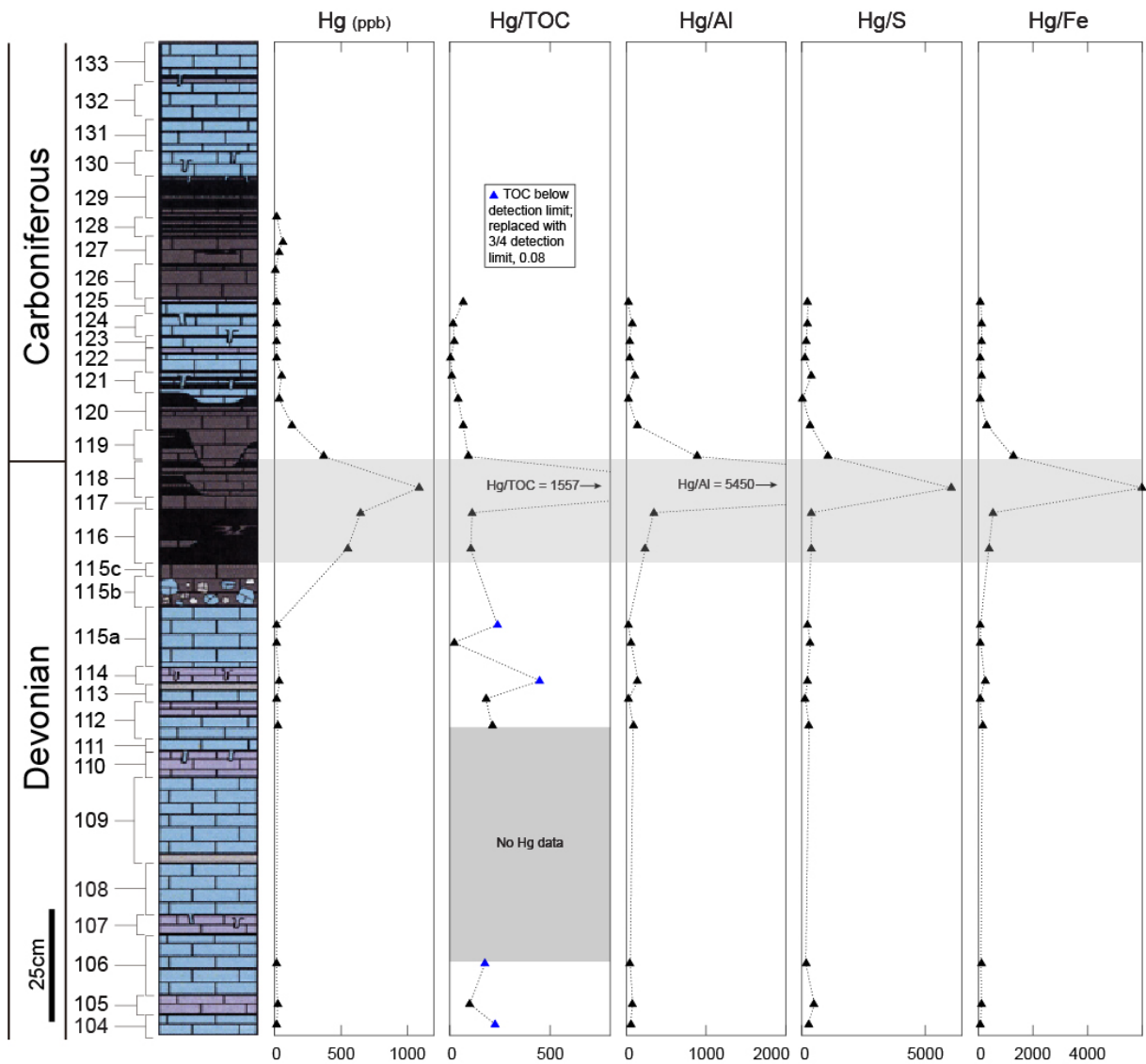
Figure II-11. Chemostratigraphy of volcanism proxies. Beds 116-120 all show total Hg above background levels, while Hg/TOC, Hg/Al, Hg/S, and Hg/Fe all show a significant spike at bed 118 (at the D-C boundary). Beds 116-118 are shaded, representing the Hangbenberg Crisis interval.

References

Algeo, T.J., 2004. Can marine anoxic events draw down the trace element inventory of seawater? Geology, 32(12), 1057-1060.

Algeo, T.J., Berner, R.A., Maynard, J.B. and Scheckler, S.E., 1995. Late Devonian oceanic anoxic events and biotic crises:"rooted" in the evolution of vascular land plants. GSA today, 5(3), 63-66.

Algeo, T.J. and Lyons, T.W., 2006. Mo–total organic carbon covariation in modern anoxic marine environments: Implications for analysis of paleoredox and paleohydrographic conditions. Paleoceanography, 21(1).

Algeo, T.J., Lyons, T.W., Blakey, R.C. and Over, D.J., 2007. Hydrographic conditions of the Devono–Carboniferous North American Seaway inferred from sedimentary Mo–TOC relationships. Palaeogeography, Palaeoclimatology, Palaeoecology, 256(3), 204-230.

Algeo, T.J. and Maynard, J.B., 2004. Trace-element behavior and redox facies in core shales of Upper Pennsylvanian Kansas-type cyclothems. Chemical Geology, 206(3–4), 289-318.

Algeo, T.J. and Maynard, J.B., 2008. Trace-metal covariation as a guide to water-mass conditions in ancient anoxic marine environments. Geosphere, 4(5), 872-887.

Algeo, T.J. and Scheckler, S.E., 1998. Terrestrial-marine teleconnections in the Devonian: links between the evolution of land plants, weathering processes, and marine anoxic events. Philosophical Transactions of the Royal Society of London. Series B: Biological Sciences, 353(1365), 113-130.

Aretz, M., 2013. Report on the workshop of the task group for defining the Devonian-Carboniferous boundary. In: M. Aretz, B. Richards, P. Kabanov and S. Nikolaeva (Eds.). Newsletter on Carboniferous Stratigraphy. International Union of Geological Sciences, Subcommission on Carboniferous Stratigraphy, pp. 31-35.

Averbuch, O. et al., 2005. Mountain building-enhanced continental weathering and organic carbon burial as major causes for climatic cooling at the Frasnian–Famennian boundary (c. 376 Ma)? Terra Nova, 17(1), 25-34.

Bábek, O., Kumpan, T., Kalvoda, J. and Grygar, T.M., 2016. Devonian/Carboniferous boundary glacioeustatic fluctuations in a platform-to-basin direction: a geochemical approach of sequence stratigraphy in pelagic settings. Sedimentary geology, 337, 81-99.

Bai, S.-l., Bai, Z.Q., Ma, X.P., Wang, D.R. and Sun, Y.L., 1994. Devonian Events and Biostratigraphy of South China. Peking University Press, Beijing, China.

Becker, R.T., Kaiser, S.I. and Aretz, M., 2016. Review of chrono-, litho-and biostratigraphy across the global Hangenberg Crisis and Devonian–Carboniferous Boundary. Geological Society, London, Special Publications, 423(1), 355-386.

Beier, J.A. and Hayes, J.M., 1989. Geochemical and isotopic evidence for paleoredox conditions during deposition of the Devonian-Mississippian New Albany Shale, southern Indiana. Geological Society of America Bulletin, 101(6), 774-782.

Bergquist, B.A., 2017. Mercury, volcanism, and mass extinctions. Proceedings of the National Academy of Sciences, 114(33), 8675–8677.

Bhatia, M.R. and Crook, K.A.W., 1986. Trace element characteristics of graywackes and tectonic setting discrimination of sedimentary basins. Contributions to Mineralogy and Petrology, 92(2), 181-193. English

Blakey, R., 2016. Devonian - 380 Ma, Global Paleogeography and Tectonics in Deep Time Series. Deep Time Maps™ Paleogeography.

Bond, D., Wignall, P.B. and Racki, G., 2004. Extent and duration of marine anoxia during the Frasnian–Famennian (Late Devonian) mass extinction in Poland, Germany, Austria and France. Geological Magazine, 141(02), 173-193.

Bond, D.P. and Wignall, P.B., 2014. Large igneous provinces and mass extinctions: An update. Geological Society of America Special Papers, 505, SPE505-02.

Brand, U., Legrand-Blain, M. and Streel, M., 2004. Biochemostratigraphy of the Devonian−Carboniferous boundary global stratotype section and point, Griotte Formation, La Serre, Montagne Noire, France. Palaeogeography, Palaeoclimatology, Palaeoecology, 205(3–4), 337-357.

Brezinski, D.K., Cecil, C.B. and Skema, V.W., 2010. Late Devonian glacigenic and associated facies from the central Appalachian Basin, eastern United States. Geological Society of America Bulletin, 122(1-2), 265-281.

Brezinski, D.K., Cecil, C.B., Skema, V.W. and Kertis, C.A., 2009. Evidence for long-term climate change in Upper Devonian strata of the central Appalachians. Palaeogeography, Palaeoclimatology, Palaeoecology, 284(3), 315-325.

Brumsack, H.-J., 2006. The trace metal content of recent organic carbon-rich sediments: implications for Cretaceous black shale formation. Palaeogeography, Palaeoclimatology, Palaeoecology, 232(2), 344-361.

Calvert, S. and Pedersen, T., 1992. Organic carbon accumulation and preservation in marine sediments: How important is anoxia. Organic matter: productivity, accumulation, and preservation in recent and ancient sediments, 533, 231-263.

Caplan, M.L., Bustin, R.M. and Grimm, K.A., 1996. Demise of a Devonian-Carboniferous carbonate ramp by eutrophication. Geology, 24(8), 715-718.

Caplan, M.L. and Bustin, R.M., 1998. Palaeoceanographic controls on geochemical characteristics of organic-rich Exshaw mudrocks: role of enhanced primary production. Organic Geochemistry, 30(2–3), 161-188.

Caplan, M.L. and Bustin, R.M., 1999. Devonian–Carboniferous Hangenberg mass extinction event, widespread organic-rich mudrock and anoxia: causes and consequences. Palaeogeography, Palaeoclimatology, Palaeoecology, 148(4), 187-207.

Caputo, M.V., de Melo, J.G., Streel, M., Isbell, J.L. and Fielding, C., 2008. Late Devonian and early Carboniferous glacial records of South America. Geological Society of America Special Papers, 441, 161-173.

Carmichael, S. K., Waters, J. A., Suttner, T. J., Kido, E., and DeReuil, A. A., 2014, A new model for the Kellwasser Anoxia Events (Late Devonian): Shallow water anoxia in an open oceanic setting in the Central Asian Orogenic Belt: Palaeogeography, Palaeoclimatology, Palaeoecology, v. 339, p. 394-403.

Carmichael, S.K. and Waters, J.A., 2015. A decade of deciphering the Late Devonian: more answers, but many more questions. In: B. Mottequin, J. Denayer, P. Koenigshof, C. Prestianni and S. Olive (Eds.), IGCP596-SDS Symposium. STRATA. Association STRATA, Brussels, Belgium, pp. 27-29.

Carmichael, S.K. et al., 2016. Climate instability and tipping points in the Late Devonian: Detection of the Hangenberg Event in an open oceanic island arc in the Central Asian Orogenic Belt. Gondwana Research, 32, 213-231.

Carmichael S, Wang Z, Waters J, Batchelor C, Coleman D, Suttner T & Kido E (2017a) Looking for the Kellwasser anoxia event in all the wrong places: the role of submarine groundwater flow (Junggar Basin, NW China): *Goldschmidt Abstracts,* 2017 558

Carmichael, S.K., Waters, J., Königshof, P., Suttner, T.J. and Kido, E., in review (this volume). Looking for the Kellwasser Event in all the "wrong" places: how does

paleogeographic and paleoenvironmental bias limit our knowledge? Submitted to Global and Planetary Change, TBA.

Charbonnier, G. et al., 2017. Mercury enrichment indicates volcanic triggering of Valanginian environmental change. Scientific Reports 7.

Cole, D., Myrow, P.M., Fike, D.A., Hakim, A. and Gehrels, G.E., 2015. Uppermost Devonian (Famennian) to Lower Mississippian events of the western U.S.: Stratigraphy, sedimentology, chemostratigraphy, and detrital zircon geochronology. Palaeogeography, Palaeoclimatology, Palaeoecology, 427, 1-19.

Copper, P., 1986. Frasnian/Famennian mass extinction and cold-water oceans. Geology, 14(10), 835-839.

Corradini, C., Kaiser, S.I., Perri, M.C. and Spalletta, C., 2011. Protognathodus (Conodonta) and its potential as a tool for defining the Devonian/Carboniferous boundary. Rivista Italiana di Paleontologia e Stratigrafia, 117(1), 15-28.

Corradini, C., Spalletta, C., Mossoni, A., Matyja, H. and Over, D.J., 2017. Conodonts across the Devonian/Carboniferous boundary: a review and implication for the redefinition of the boundary and a proposal for an updated conodont zonation. Geological Magazine, 154(4), 888-902.

Cramer, B., Saltzman, M., Day, J.E. and Witzke, B.J., 2008. Record of the Late Devonian Hangenberg global positive carbon-isotope excursion in an epeiric sea setting: carbonate production, organic-carbon burial and paleoceanography during the Late Famennian. Dynamics of Epeiric Seas, Geological Association of Canada Special 838 Paper, 48, 103-118.

De Vleeschouwer, D., Crucifix, M., Bounceur, N. and Claeys, P., 2014. The impact of astronomical forcing on the Late Devonian greenhouse climate. Global and Planetary Change, 120, 65-80.

De Vleeschouwer, D. et al., 2017. Timing and pacing of the Late Devonian mass extinction event regulated by eccentricity and obliquity. Nature communications, 8(1).

De Vleeschouwer, D., Königshof, P. and Claeys, P., 2018. Reading time and paleoenvironmental change in the Emsian–Eifelian boundary GSSP section (Wetteldorf, Germany): A combination of cyclostratigraphy and facies analysis. Newsletters on Stratigraphy, 51(2), 209-226.

De Vleeschouwer, D. et al., 2013. The astronomical rhythm of Late-Devonian climate change (Kowala section, Holy Cross Mountains, Poland). Earth and Planetary Science Letters, 365, 25-37.

Doan, T.N. and Tong-Dzuy, T., 2006. Upper Paleozoic. In: T. Tong-Dzuy and V. Khuc (Eds.), Stratigraphic Units of Vietnam. Vietnam National University Publishing House, Hanoi, Vietnam, pp. 201-244.

Dymond, J., Suess, E. and Lyle, M., 1992. Barium in deep-sea sediment: A geochemical proxy for paleoproductivity. Paleoceanography, 7(2), 163-181.

Elderfield, H. and Greaves, M.J., 1982. The rare earth elements in seawater. Nature, 296, 214-219.

Ernst, W., 1970. Geochemical facies analysis, 11. Elsevier, 152 pp.

Flajs, G. and Feist, R., 1988. Index conodonts, trilobites and environment of the Devonian-Carboniferous boundary beds at La Serre (Montagne Noire, France). Courier Forschungsinstitut Senckenberg, 100, 53-107.

Formolo, M.J., Riedinger, N. and Gill, B.C., 2014. Geochemical evidence for euxinia during the Late Devonian extinction events in the Michigan Basin (USA). Palaeogeography, Palaeoclimatology, Palaeoecology, 414, 146-154.

German, C.R. and Elderfield, H., 1990. Application of the Ce anomaly as a paleoredox indicator; the ground rules. Paleoceanography, 5(5), 823-833.

Hammer, Ø., Harper, D. and Ryan, P., 2001. PAST: Paleontological Statistics Software Package for Education and Data Analysis, Palaeontologia Electronica, pp. 2009.

Hatch, J. and Leventhal, J., 1992. Relationship between inferred redox potential of the depositional environment and geochemistry of the Upper Pennsylvanian (Missourian) Stark Shale Member of the Dennis Limestone, Wabaunsee County, Kansas, USA. Chemical Geology, 99(1-3), 65-82.

Hoffman, D. et al., 1998. Regional and stratigraphic variation in bottomwater anoxia in offshore core shales of Upper Pennsylvanian cyclothems from the Eastern Midcontinent Shelf (Kansas), USA. In: J. Schieber, W. Zimmerle and P.S. Sethi (Eds.), Shales and Mudstones. Schweizerbartische Verlagsbuchhandlung, Stuttgart, Germany, pp. 243-269.

Isaacson, P. et al., 2008. Late Devonian–earliest Mississippian glaciation in Gondwanaland and its biogeographic consequences. Palaeogeography, Palaeoclimatology, Palaeoecology, 268(3), 126-142.

Isaacson, P., Hladil, J., Shen, J., Kalvoda, J. and Grader, G., 1999. Late Devonian (Famennian) glaciation in South America and marine offlap on other continents. Abhandlungen-Geologischen Bundesanstalt, 54, 239-258.

Jones, B. and Manning, D.A., 1994. Comparison of geochemical indices used for the interpretation of palaeoredox conditions in ancient mudstones. Chemical Geology, 111(1), 111-129.

Kaiser, S.I., Aretz, M. and Becker, R.T., 2015. The global Hangenberg Crisis (Devonian–Carboniferous transition): review of a first-order mass extinction. Geological Society, London, Special Publications, 423, SP423. 9.

Kido, E, Suttner, T.J., Waters, J.A., Yarinpil, A., Gonchigdorj, S., Atwood, J.W., and Webster, G.D, 2013. Devonian deposits of the Baruunhuurai Terrane, western Mongolia (IGCP 596 Field Workshop). Episodes, 36(4), 242-254.

Komatsu, T. et al., 2014. Devonian–Carboniferous transition containing a Hangenberg Black Shale equivalent in the Pho Han Formation on Cat Ba Island, northeastern Vietnam. Palaeogeography, Palaeoclimatology, Palaeoecology, 404, 30-43.

Komatsu, T. et al., 2012. Devonian–Carboniferous transition in the pho han formation on Cat Ba Island, northeastern Vietnam. The Journal of the Geological Society of Japan, 118(6), V-VI.

Krencker, F. et al., 2014. The middle Toarcian cold snap: trigger of mass extinction and carbonate factory demise. Global and Planetary Change, 117, 64-78.

Kumpan, T., Bábek, O., Kalvoda, J., Frýda, J. and Matys Grygar, T., 2014a. A high-resolution, multiproxy stratigraphic analysis of the Devonian–Carboniferous boundary sections in the Moravian Karst (Czech Republic) and a correlation with the Carnic Alps (Austria). 941 Geological Magazine, 151(02), 201-215.

Kumpan, T., Bábek, O., Kalvoda, J., Matys Grygar, T. and Frýda, J., 2014b. Sea-Level and Environmental Changes Around the Devonian–Carboniferous Boundary in the Namur–Dinant Basin (S Belgium, NE France): A Multi-proxy Stratigraphic Analysis of Carbonate Ramp Archives and its Use in Regional and Interregional Correlations. Sedimentary Geology, 311, 43-59.

Lyons, T.W., Werne, J.P., Hollander, D.J. and Murray, R., 2003. Contrasting sulfur geochemistry and Fe/Al and Mo/Al ratios across the last oxic-to-anoxic transition in the Cariaco Basin, Venezuela. Chemical Geology, 195(1), 131-157.

Marynowski, L. et al., 2012. Deciphering the upper Famennian Hangenberg Black Shale depositional environments based on multi-proxy record. Palaeogeography, Palaeoclimatology, Palaeoecology, 346, 66-86.

McGhee, G.R., 2001. Extinction: Late Devonian Mass Extinction, eLS. John Wiley & Sons, Ltd, 10.1002/9780470015902.a0001653.pub3.

McGhee, G.R., 2005. Modelling Late Devonian extinction hypotheses. In: D.J. Over, J.R. Morrow and P.B. Wignall (Eds.), Developments in Palaeontology and Stratigraphy. 1647 Elsevier, 20, pp. 37-50.

McGhee, G.R., Clapham, M.E., Sheehan, P.M., Bottjer, D.J. and Droser, M.L., 2013. A new ecological-severity ranking of major Phanerozoic biodiversity crises. Palaeogeography, Palaeoclimatology, Palaeoecology, 370(0), 260-270.

McKay, J. and Pedersen, T., 2008. The accumulation of silver in marine sediments: A link to biogenic Ba and marine productivity. Global Biogeochemical Cycles, 22(4).

Metcalfe, I., 2009. Late Palaeozoic and Mesozoic tectonic and palaeogeographical evolution of SE Asia. Geological Society, London, Special Publications, 315(1), 7-23.

Middelburg, J. and Levin, L., 2009. Coastal hypoxia and sediment biogeochemistry. Biogeosciences Discussions, 6(2), 3655-3706.

Morad, S. and Felitsyn, S., 2001. Identification of primary Ce-anomaly signatures in fossil biogenic apatite: implication for the Cambrian oceanic anoxia and phosphogenesis. Sedimentary Geology, 143(3), 259-264.

Paproth, E., Feist, R. and Flajs, G., 1991. Decision on the Devonian-Carboniferous boundary stratotype. Episodes, 14(4), 331-336.

Percival, L.M.E. et al., 2017. Mercury evidence for pulsed volcanism during the end-Triassic mass extinction. Proceedings of the National Academy of Sciences of the United States of America, 114(30), 7929-7934.

Perkins, R.B., Piper, D.Z. and Mason, C.E., 2008. Trace-element budgets in the Ohio/Sunbury shales of Kentucky: Constraints on ocean circulation and primary productivity in the Devonian–Mississippian Appalachian Basin. Palaeogeography, Palaeoclimatology, Palaeoecology, 265(1–2), 14-29.

Piper, D.Z. and Calvert, S.E., 2009. A marine biogeochemical perspective on black shale deposition. Earth-Science Reviews, 95(1–2), 63-96.

Qie, W. et al., 2015. Local overprints on the global carbonate δ13C signal in Devonian–Carboniferous boundary successions of South China. Palaeogeography, Palaeoclimatology, Palaeoecology, 418(0), 290-303.

Racki, G., 2005. Toward understanding Late Devonian global events: few answers, many questions. In: D.J. Over, J.R. Morrow and P.B. Wignall (Eds.), Understanding Late Devonian and Permian-Triassic Biotic and Climatic Events: Towards an Integrated Approach, pp. 5-36.

Racki, G., Rakociński, M., Marynowski, L. and Wignall, P.B., 2018. Mercury enrichments and the Frasnian-Famennian biotic crisis: A volcanic trigger proved? Geology.

Raup, D.M., and Sepkiski, J.J.Jr., 1982, Mass extinctions in the marine fossil record. Science, 215, 1501-1503.

Rimmer, S.M., 2004. Geochemical paleoredox indicators in Devonian–Mississippian black shales, Central Appalachian Basin (USA). Chemical Geology, 206(3–4), 373-391.

Rowan, C.J., Roberts, A.P. and Broadbent, T., 2009. Reductive diagenesis, magnetite dissolution, greigite growth and paleomagnetic smoothing in marine sediments: A new view. Earth and Planetary Science Letters, 277(1), 223-235.

Sandberg, C.A., Morrow, J.R. and Ziegler, W., 2002. Late Devonian sea-level changes, catastrophic events, and mass extinctions. Geological Society of America Special Papers, 356, 473-487.

Sandberg, C.A., Ziegler, W., Leuteritz, K. and Brill, S.M., 1978. Phylogeny, speciation, and zonation of Siphonodella (Conodonta, upper Devonian and lower Carboniferous). Newsletters on Stratigraphy, 102-120.

Schmitz, B., Charisi, S.D., Thompson, E.I. and Speijer, R.P., 1997. Barium, SiO2 (excess), and P2O5 as proxies of biological productivity in the Middle East during the Palaeocene and the latest Palaeocene benthic extinction event. Terra Nova, 9(2), 95-99.

Sepkoski, J.J., 1996. Patterns of Phanerozoic extinction: a perspective from global data bases. In: O.H. Walliser (Ed.), Global events and event stratigraphy in the Phanerozoic. Springer-Verlag, Berlin, Berlin, pp. 35-51.

Smith, M.G. and Bustin, R.M., 1998. Production and preservation of organic matter during deposition of the Bakken Formation (Late Devonian and Early Mississippian), Williston Basin. Palaeogeography, Palaeoclimatology, Palaeoecology, 142(3–4), 185-200.

Spalletta, C., Perri, M.C., Over, D.J. and Corradini, C., 2017. Famennian (Upper Devonian) conodont zonation: revised global standard. Bulletin of Geosciences, 92(1), 31-57.

Streel, M., Caputo, M.V., Loboziak, S. and Melo, J.H.G., 2000. Late Frasnian–Famennian climates based on palynomorph analyses and the question of the Late Devonian glaciations. Earth-Science Reviews, 52(1), 121-173.

Suttner, T.J., Kido, E., Chen, X.Q., Mawson, R., Waters, J.A., Frýda, J., Mathieson, D., Molloy, P.D., Pickett, J., Webster, G.D., Frýdová, B., 2014. Stratigraphy and facies development of the marine Late Devonian near the Boulongour Reservoir, northwest Xinjiang, China. Journal of Asian Earth Sciences, 80, 101–118.

Suttner, T., Kido, E., Ariunchimeg, Y., Sersmaa, G., Waters, J., Carmichael, S.K., Batchelor, C., Ariuntogos, M., Husková, Slavik, L., Valenzuela-Rios, J.I., Liao, J., and Gatovsky, Y., 2018. Conodonts from Late Devonian island arc settings (Baruunhuurai Terrane, western Mongolia). Palaeogeography, Palaeoclimatology, Palaeoecology (accepted).

Ta Hoa, P. and Doan, T.N., 2005. Preliminary studies on the Devonian–Carboniferous boundary at the Nam Cat Ba section, Hai Phong Province. Journal Science Vietnam National University, 21, 38-47. (in Vietnamese with English abstract)

Ta Hoa, P. and Doan, T.N., 2007. Discussion on the Devonian/ Carboniferous boundary at the south of Cat Ba Island. Journal Geological Series A, 298, 12-17. (in Vietnamese with English abstract)

Thibodeau, A.M. and Bergquist, B.A., 2017. Do mercury isotopes record the signature of massive volcanism in marine sedimentary records? Geology, 45(1), 95-96.

Thomas, R.M., Carmichael, S.K., Waters, J.A. and Batchelor, C.J., 2017. Peeking out of the basins: looking for the Late Devonian Kellwasser Event in the open ocean in the Central Asian Orogenic Belt, southwestern Mongolia, American Geophysical Union Fall Meeting, New Orleans, LA, pp. PP23A-1299.

Tribovillard, N., Algeo, T.J., Lyons, T. and Riboulleau, A., 2006. Trace metals as paleoredox and paleoproductivity proxies: An update. Chemical Geology, 232(1–2), 12-32.

Ver Straeten, C.A., Brett, C.E. and Sageman, B.B., 2011. Mudrock sequence stratigraphy: A multi-proxy (sedimentological, paleobiological and geochemical) approach, Devonian Appalachian Basin. Palaeogeography, Palaeoclimatology, Palaeoecology, 304(1), 54-73.

Walliser, O.H., 1984. Pleading for a natural D/C boundary. Courier Forschungsinstitut Senckenberg, 67, 241-246.

Walliser, O.H., 1996. Global events in the Devonian and Carboniferous, Global events and event stratigraphy in the Phanerozoic. Springer, pp. 225-250.

Wang, P., Huang, Y., Wang, C., Feng, Z. and Huang, Q., 2013. Pyrite morphology in the first member of the Late Cretaceous Qingshankou Formation, Songliao Basin, Northeast China. Palaeogeography, Palaeoclimatology, Palaeoecology, 385, 125-136.

Wang, Z., Becker, R.T, Aboussalam, Z.S., Hartenfels, S., Joachimski, M.M., and Gong, Y.M., 2016. Conodont and carbon isotope stratigraphy near the Frasnian/Famennian (Devonian) boundary at Wulankeshun, Junggar Basin, NW China. Palaeogeography, Palaeoclimatology, Palaeoecology, 448, 279-297.

Wignall, P. and Newton, R., 1998. Pyrite framboid diameter as a measure of oxygen deficiency in ancient mudrocks. American Journal of Science, 298(7), 537-552.

Wignall, P.B. and Myers, K.J., 1988. Interpreting benthic oxygen levels in mudrocks: a new approach. Geology, 16(5), 452-455.

Wilde, P., Quinby-Hunt, M.S. and Erdtmann, B.-D., 1996. The whole-rock cerium anomaly: a potential indicator of eustatic sea-level changes in shales of the anoxic facies. Sedimentary Geology, 101(1), 43-53.

Wilkin, R. and Barnes, H., 1997. Formation processes of framboidal pyrite. Geochimica et Cosmochimica Acta, 61(2), 323-339.

Wilkin, R., Barnes, H. and Brantley, S., 1996. The size distribution of framboidal pyrite in modern sediments: An indicator of redox conditions. Geochimica et Cosmochimica Acta, 60(20), 3897-3912.

Wilkin, R.T., Arthur, M.A. and Dean, W.E., 1997. History of water-column anoxia in the Black Sea indicated by pyrite framboid size distributions. Earth and Planetary Science Letters, 148(3), 517-525.

Wright, J., Schrader, H. and Holser, W.T., 1987. Paleoredox variations in ancient oceans recorded by rare earth elements in fossil apatite. Geochimica et Cosmochimica Acta, 51(3), 631-644.

Xiao, W., Huang, B., Han, C., Sun, S. and Li, J., 2010. A review of the western part of the Altaids: a key to understanding the architecture of accretionary orogens. Gondwana Research, 18(2), 253-273.

Ziegler, W. and Sandberg, C.A., 1990. The Late Devonian standard conodont zonation. Courier Forschungsinstitut Senckenberg, 121, 1-115.